Title
Multi-Scale Spatial Variations in Pacific Mantle Seismic Anisotropy: Constraints on Plate Evolution and Asthenospheric Flow

Journal
Journal of Geophysical Research: Solid Earth, 131(8)

ISSN
2169-9313

Authors
Phillips, Joseph H
Gaherty, James B
Russell, Joshua B
et al.

Publication Date
2026-08-01

DOI
10.1029/2025jb033545

AGU ADVANCING EARTH AND SPACE SCIENCES

JGR Solid Earth

RESEARCH ARTICLE
10.1029/2025JB033545

Key Points:

- New regional models of seismic anisotropy reveal lateral and depth-dependent variations in Pacific mantle anisotropy that are not well-captured in global models
- Strong asthenospheric anisotropy reflects plate-driven shear in a sub-lithospheric channel and pressure- and/or buoyancy-driven deformation at greater depth
- Lithospheric anisotropy is very heterogeneous in strength and direction with respect to spreading, indicating competing sources of ridge-related deformation

Supporting Information:

Supporting Information may be found in the online version of this article.

Correspondence to:

J. B. Russell,
jbrussel@syr.edu

Citation:

Phillips, J. H., Gaherty, J. B., Russell, J. B., Eilon, Z. C., Forsyth, D. W., & Byrnes, J. S. (2026). Multi-scale spatial variations in Pacific mantle seismic anisotropy: Constraints on plate evolution and asthenospheric flow. *Journal of Geophysical Research: Solid Earth*, *131*, e2025JB033545. https://doi.org/10.1029/2025JB033545

Received 3 DEC 2025
Accepted 3 AUG 2026

Author Contributions:

Conceptualization: James B. Gaherty
Writing – original draft: Joseph H. Phillips
Writing – review & editing: Joseph H. Phillips, James B. Gaherty, Joshua B. Russell, Zachary C. Eilon, Donald W. Forsyth, Joseph S. Byrnes

Multi-Scale Spatial Variations in Pacific Mantle Seismic Anisotropy: Constraints on Plate Evolution and Asthenospheric Flow

Joseph H. Phillips[1], James B. Gaherty[1], Joshua B. Russell[2], Zachary C. Eilon[3], Donald W. Forsyth[4], and Joseph S. Byrnes[5]

[1]Northern Arizona University, Flagstaff, AZ, USA, [2]Syracuse University, Syracuse, NY, USA, [3]University of California at Santa Barbara, Santa Barbara, CA, USA, [4]Brown University, Providence, RI, USA, [5]University of Texas at Dallas, Richardson, TX, USA

Abstract We present array-scale (~500 × 500 km) anisotropic shear-velocity models from two Pacific ocean-bottom seismometer (OBS) arrays of the OBS Research in the Convecting Asthenosphere (ORCA) experiment: Young ORCA (~43 Ma) and Old ORCA (~90 Ma). Rayleigh-wave phase velocities spanning 5–150 s are combined with Love-wave phase velocities from 5 to 10 s to constrain (V_{SV}) and its azimuthal variation (G) to 300-km depth, and radial anisotropy $\xi = (V_{SH}/V_{SV})^2$ azimuthal (V_{SH}) parameter E to ~50 km depth. Both sites show a lithospheric lid over a low-velocity zone, with lid thickness correlating with plate age, and positive ξ through the crust and upper lithosphere. Young ORCA has moderate lithospheric azimuthal anisotropy ($|G| \sim 3\%$) consistent with spreading-parallel corner flow to ~30–50 km, while Old ORCA displays weak (~1%–2%), laterally variable lithospheric anisotropy that is rotated ~30° from fossil spreading, suggesting perturbed corner-flow processes at the ridge. A sharp fabric change at ~70-km depth in Old ORCA marks the lithosphere-asthenosphere boundary (LAB), consistent with dehydration-controlled plate thickness. Beneath the lithosphere, both regions exhibit strong asthenospheric anisotropy ($|G| \sim 3\%$) with fast axes subparallel to absolute plate motion in a narrow channel between ~70 and 200 km depth, suggesting plate-induced shear within a weak shallow asthenosphere. At greater depths, anisotropy amplitudes decrease and azimuths rotate (N–S beneath Young; NW–SE beneath Old), consistent with superposed pressure or buoyancy-driven flow in the deeper asthenosphere. Global models of azimuthal anisotropy under-predict strength, depth variability, and rotation of fabric, underscoring the utility of dense OBS arrays for resolving smaller-scale deformation processes within the oceanic lithosphere-asthenosphere system.

Plain Language Summary We used seafloor seismometers to "listen" to naturally sourced seismic waves traveling through the Pacific mantle beneath two areas of different ages: ~43 million years (Young ORCA) and ~90 million years (Old ORCA). Subtle changes in wave speed with direction reveal how mantle minerals are lined up by past and present mantle flow. Within the near-surface Pacific plate ("lithosphere"), the younger site records a strong fabric aligned with the direction plates spread apart when that seafloor formed. The older site shows weaker, rotated fabric, pointing to more complicated spreading or later modification. Deeper beneath the plate ("asthenosphere"), both places show strong alignment that mostly follows today's motion of the Pacific plate over the mantle, consistent with the plate ("lithosphere") shearing the layer ("asthenosphere") beneath it. We also identify the transition between these layers at ~50 km depth under the younger site and ~70–75 km under the older site. When we compare our local results with global maps, the global maps tend to underestimate the strength and variability of this fabric. Direct ocean-bottom observations are therefore crucial for revealing small-scale mantle processes that larger-scale studies smooth out.

1. Introduction

The lithosphere-asthenosphere system is integral to Earth's tectonic evolution. Seismic anisotropy, characterized by variation in seismic wave speeds depending on wave polarization and propagation direction, offers constraints on the dynamics of this system. Anisotropy in the upper mantle primarily results from the alignment of olivine crystals by viscous deformation (Auer et al., 2015; Forsyth, 1975; Hess, 1964; Karato et al., 2008; Long & Becker, 2010; Montagner & Tanimoto, 1990). Ocean basins record past and present mantle-convective processes, including seafloor spreading (Eakin et al., 2018; Eilon & Abers, 2017; Gu et al., 2005) and associated volcanism at mid-ocean ridges (Forsyth et al., 2006), lithospheric cooling (Korenaga et al., 2021), sub-plate convection

(Ballmer et al., 2010; Buck, 1985; Conrad & Hager, 2001; Eilon et al., 2022; Kang et al., 2023), hotspot and intraplate volcanism (Ballmer et al., 2007, 2011; Laske et al., 2011), and subduction-induced flow and faulting (Bodmer et al., 2015; Hawley et al., 2016; Long & Silver, 2009; Nakajima & Hasegawa, 2004). The spatial, temporal (i.e., age-dependent), and depth extent of seismic anisotropy in ocean basins provides key constraints on these various geodynamic processes.

Early observations of anisotropy in seismic refraction data from the ocean basins (e.g., Hess, 1964; Raitt et al., 1969) suggest that seafloor spreading produces mineral fabrics in the uppermost mantle that align with the plate-spreading direction. As incipient lithosphere forms near the mid-ocean ridge (MOR), shear deformation associated with corner flow induces a lattice preferred orientation or crystallographic preferred orientation (CPO)—if deformation takes place by dislocation creep—of olivine crystals with fast *a*-axes aligned parallel to the spreading direction (e.g., Blackman et al., 1996, 2017; Blackman & Kendall, 2002; Kaminski & Ribe, 2002; Ribe, 1989). As the plate ages, this fabric freezes into the lithosphere recording paleo-deformation conditions near the MOR (fossil-spreading direction; FSD). Measurements from both active- and passive-source datasets show that, in many regions, uppermost mantle fast axes do conform to the FSD, as inferred from magnetic anomalies and/or seafloor topography (e.g., Eddy et al., 2019; Gaherty et al., 2004; Laske et al., 2026; Lin et al., 2016; Mark et al., 2019; Nishimura & Forsyth, 1989; Russell, Gaherty, et al., 2019; Takeo et al., 2014). However, a growing number of observations indicate significant deviations from FSD in a variety of paleo-spreading environments (Kawano et al., 2023; Russell & Gaherty, 2021; Saikia et al., 2021; Takeo et al., 2018; VanderBeek & Toomey, 2017); these observations are providing unique new constraints on the complexity of mid-ocean ridge dynamics and plate evolution.

Motion of the rigid lithosphere, relative to the deep mantle, leads to shearing of the weaker asthenospheric mantle and formation of olivine CPO (Zhang & Karato, 1995). Since this CPO reflects relative shear, its fast direction is expected to approximately agree with the direction of absolute plate motion (APM) in a hotspot or no-net-rotation reference frame, if the plate motion is the dominant source of deformation(e.g., Gripp & Gordon, 2002; Kreemer et al., 2014). This observation is broadly confirmed by plate- and global-scale shear-wave tomography models (Becker et al., 2014; Beghein et al., 2014; Debayle et al., 2016; Debayle & Ricard, 2012, 2013; Eddy et al., 2019, 2022; French & Romanowicz, 2014; Montagner, 2002; Montagner & Tanimoto, 1991; Nishimura & Forsyth, 1989). However, more localized analyses document environments where asthenospheric anisotropy differs substantially from APM (Becker et al., 2014; Lin et al., 2016; Takeo et al., 2018; Russell, Gaherty, et al., 2019) presumably due to heterogeneous mantle flow processes such as pressure-driven flow (e.g., Nagel et al., 2008; Semple & Lenardic, 2018; Wang et al., 2025) or small-scale convection (e.g., Ballmer et al., 2010). These exceptions to the rule may elucidate local stress conditions that drive flow, and have implications for associated mantle properties (temperature, rheology) and plate evolution.

While these localized anisotropy estimates clearly require deformation beyond that produced by FSD and APM, the sparse sampling and diverse type and quality of the anisotropy estimates makes it difficult to discern the details of the controlling processes, including absolute and relative plate velocity, heterogeneous mantle flow, and intraplate aging and modification. In this study, we present new models of shear-wave velocity and anisotropy spanning the lithosphere-asthenosphere system in two parts of the Pacific basin, at plate ages of approximately 43 and 90 Ma. These regions are characterized by plates with distinctly different spreading systems, and sample disparate asthenosphere regimes where apparent small-scale sub-lithospheric convection is documented (Eilon et al., 2022; Hariharan et al., 2025). Our anisotropy models make use of surface-wave observations recorded across localized broadband ocean-bottom seismograph (OBS) arrays of approximately 500×500 km^2 aperture, which provide robust estimates of phase velocities and their azimuthal variation within each array footprint. These data provide unusually complete constraints on azimuthally anisotropic shear velocity parameters from the seafloor to ~300 km depth, as well as radial anisotropy through the crust and upper ~50 km of the mantle lithosphere in each region. The anisotropic models from this study, taken alongside results from other OBS experiments in the Pacific, Atlantic, and Indian Oceans, document dramatic heterogeneity in both lithospheric and asthenospheric anisotropy. These relatively high-resolution estimates of anisotropy are used to evaluate contributions of smaller-scale deformation processes, as well as the degree to which global estimates robustly capture the dominant mechanisms of asthenospheric deformation. Collectively, these findings provide unique new constraints on dynamical processes at mid-ocean ridges and within and beneath oceanic plates.

AGU ADVANCING EARTH AND SPACE SCIENCES
Journal of Geophysical Research: Solid Earth
10.1029/2025JB033545

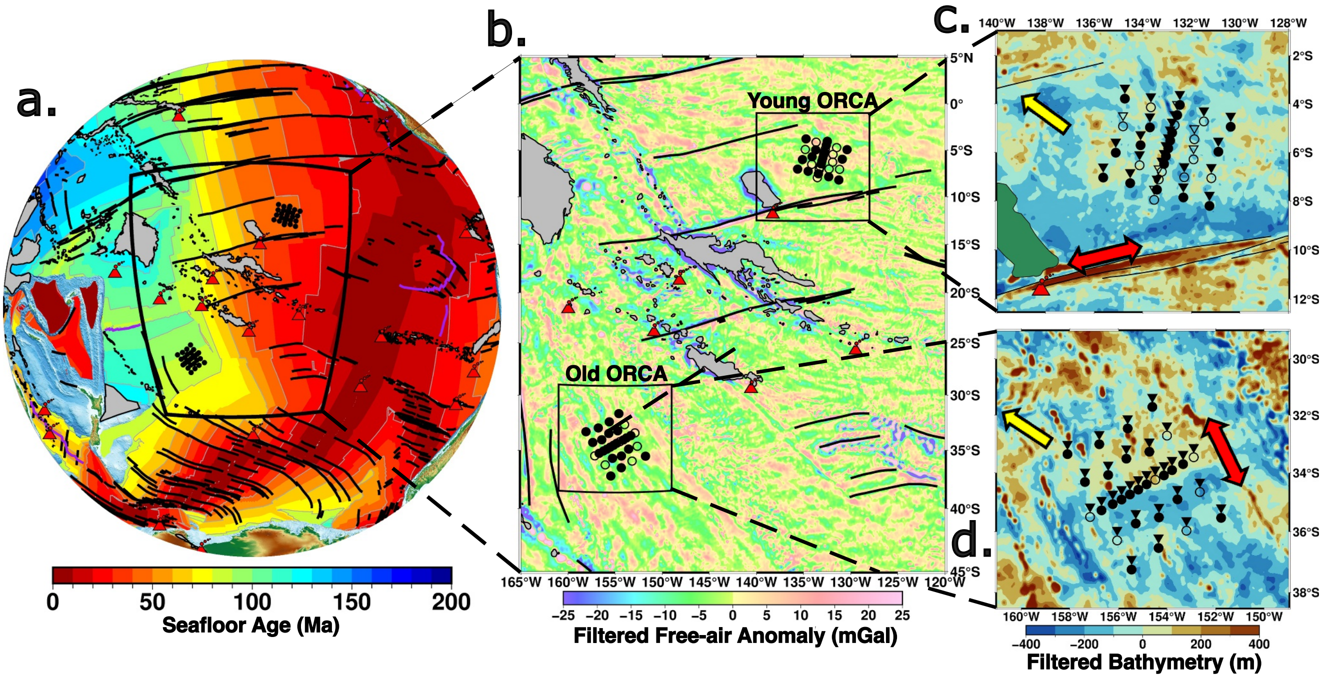

Figure 1. Maps showing OBS locations for Young and Old ORCA arrays. (a) Circles indicate Young and Old ORCA OBS arrays plotted on the seafloor age model of Seton et al. (2020). Large igneous provinces shown as gray polygons (Coffin et al., 2006). Hotspot locations identified by red volcano symbols (Jackson et al., 2021). Seafloor fracture zones are thin black lines. Extinct ridges identified by thin purple lines, most notably the Osbourn trough northwest of Old ORCA (Matthews et al., 2011). Black box shows map boundaries for Young and Old ORCA array deployments. (b) Zoom-in view of the south-west Pacific, with OBS stations plotted over the free-air gravity anomaly (Sandwell et al., 2021) filtered with a 40 km gaussian convolution filter following Eilon et al. (2022). (c, d) Zoom-in views of Young (top) and Old (bottom) ORCA arrays with three-component seismometers (circles) and differential pressure gauge (triangles). Empty circles are seismometers with poor data recovery, see Eilon et al. (2021). Yellow arrows show absolute plate motion in a no-net-rotation reference frame (Kreemer et al., 2014) and red double headed arrows show approximate fossil-spreading direction (FSD) within each array. Background bathymetry is de-meaned and filtered in the same way as free-air anomaly in (b).

2. ORCA Broadband Experiment

The OBS Research into Convecting Asthenosphere (ORCA) experiment consists of two separate broadband OBS arrays deployed for (non-overlapping) 12–13 month periods in the central and south Pacific (Figure 1a). Each deployment utilized 30 broadband OBS systems, comprising a three-component Trillium 240 seismometer and a differential pressure gauge (DPG), deployed in similar 500 × 500 km^2 footprints (Eilon et al., 2021). Each array incorporated a linear subarray of 12 instruments deployed with ∼40–50 km spacing, embedded within a two-dimensional distribution of stations with ∼100–125 km spacing. In each case, the central subarray was oriented perpendicular to lineations in the gravity field (Figure 1), the enigmatic source of which provided a primary motivation for the experiment (Eilon et al., 2021, 2022). The broader 2-D array coverage mimics the successful NoMelt experiment from the central Pacific, which yielded high quality surface-and body-wave analyses of velocity, anisotropy, and attenuation within the lithosphere-asthenosphere system (Lin et al., 2016; Russell, Gaherty, et al., 2019; Ma et al., 2020; Mark et al., 2021). ORCA OBS positions on the seafloor were determined to within <5 m using ranging from the ship interpreted with the OBSrange software package (Russell, Eilon, & Mosher, 2019). OBS orientations for the horizontal components were determined using the DLOPy method (Doran & Laske, 2017) with earthquakes >6.5 M_w. In the instances of clock failure prior to OBS recovery, clock drift and resulting timing were estimated following (Hable et al., 2018). Details on instrument failures, data quality, and overall availability and usability are presented by Eilon et al. (2021). Here we provide a short summary of unique aspects of each array site and data set.

2.1. Young ORCA

Young ORCA was deployed from April 2018 to May 2019, centered ∼800 km northeast of the Marquesas Islands and midway between the Galapagos and Marquesas fracture zones on 40–45 Ma seafloor (Seton et al., 2020).

Fossil spreading rates appear to be fast, with half-rates of 100–120 mm/yr (Müller et al., 2008), and the fossil spreading direction (FSD) is ∼75° based on the orientation of the bounding fracture zones. Local absolute plate motion (APM) is 294° in a no-net-rotation reference frame (Kreemer et al., 2014). The average seafloor depth is 4,620 m, with height variations dominated by abyssal hill topography with ∼100-m root-mean-square variability. The abyssal-hill orientation varies between 60° and 90° relative to the inferred FSD (Figure S1a in Supporting Information S1), with local variations suggesting the existence of small overlapping spreading centers and/or oblique spreading at the time of formation of the seafloor, and the array footprint is also characterized by distinct seamounts and tectonic or volcanic ridges that reach depths as shallow as 3,570 m. On a regional scale, seafloor depths in the southwestern portion of the array are slightly shallower, presumably due to the influence of the Marquesas hotspot swell. A sequence of mechanical, power, and datalogger errors resulted in heterogeneous data return (Eilon et al., 2021), with approximately 68% total useable data recovery, some of which has very high noise characteristics due to sensor issues. These issues affected the longer period (>30 s) horizontal component data most strongly.

2.2. Old ORCA

Old ORCA was deployed from November 2019 to December 2020, centered on ancient Pacific lithosphere approximately 2,500 km ENE of New Zealand and 1,900 km SSW of Tahiti. The age of the site lies within the Cretaceous Normal Superchron (e.g., Yoshimura, 2022) and lacks magnetic anomalies and major bounding fracture zones, but high-resolution bathymetry data display clear abyssal hill morphology striking ∼60°–70° (Figure S1b in Supporting Information S1), implying a FSD of 330°–340° (Figure 1d). APM is 300° relative to a no-net rotation reference frame (Kreemer et al., 2014). Average seafloor depth is 5,280 m, with RMS variability of 240 m produced by a combination of abyssal-hill topography and volcanic ridges and seamounts. Seamounts and volcanic ridges are more abundant in the northern half of the array, with average bathymetric depths that are ∼200 m shallower to the northwest of the central line of OBSs (5,230 m) than to the southeast (5,436 m) (Figure 1c). This bathymetry change is coincident with a ∼10 mGal change in free-air anomaly (Figure 1b) and Bouguer anomaly (Figures S1c and S1d in Supporting Information S1), which, assuming Airy isostasy, implies an approximately 1-km increase in average crustal thickness from SE to NW within the array.

Due to the lack of magnetic anomalies, several different seafloor age models and reconstructions have been proposed for the region surrounding the Old ORCA site. The Müller et al. (2008) global age model places the site on 120–130 Ma ocean crust formed during slow SSE-oriented spreading at the now stalled-out Osbourn Trough located NW of the site. This model requires abrupt discontinuities in seafloor age to the east and south of the site but is generally consistent with the ENE trend of the abyssal hill topography. The updated global seafloor age model (Seton et al., 2020) utilizes a more continuous parameterization that reduces those discontinuities, and it predicts that the site sits on 90–100 Ma seafloor with a complex ancient spreading history. The age isochrons in that model are variable with NNE-SSW to NNW-SSE orientation, inconsistent with the clear ENE-WSW abyssal-hill fabric observed in the region. Eagles et al. (2004), Eagles (2006) utilized dates from ocean-drilling cores and high-resolution bathymetry and gravity constraints to develop a regional age model for the relict Osbourn and Pacific-Phoenix spreading systems. They interpret a NW-trending bathymetric feature west of Old ORCA to bound the eastern edge of Osbourn spreading, placing the site on ∼85–95 Ma seafloor formed by relatively fast NNW-spreading at the former Pacific-Phoenix ridge (Eagles et al., 2004; Larter et al., 2002; Mortimer et al., 2019). This model predicts a ridge orientation that is consistent with the strike of abyssal hill fabric. The RMS of the abyssal hill fabric at Old ORCA of approximately 75–110 m (calculated in the southeastern portion of the array with minimal seamount density) is more consistent with faster spreading (>70 mm/yr half spreading rate), also favoring the Eagles et al. (2004) model (Goff & Arbic, 2010). For our purposes, we infer that the plate here is old (at least ∼85 Ma, and perhaps as old as ∼125 Ma), formed via NNW-SSE spreading younging to the SSE with an orientation consistent with abyssal-hill fabric (FSD ∼330°–340°).

Overall data return for Old ORCA was excellent, with nearly 100% recovery of DPG data, and nearly complete three-component seismic data at 23 of 30 stations. Complete failure of the datalogger for the seismic channels occurred at seven stations; otherwise, only one horizontal channel (NN02) was anomalously noisy (Eilon et al., 2021).

3. Surface-Wave Analysis

We analyze seismic surface waves recorded across a wide period range (5–150 s) to determine the shear velocity and anisotropy within each array. Ambient-noise Green's functions extracted from the vertical-component (see Section 3.2) provide Rayleigh wave phase velocities in the 4–25 s band (Adimah et al., 2024; Russell & Gaherty, 2021), and those from tangential-component records provide Love-wave phase velocities in the 4–8 s band (Russell, Gaherty, et al., 2019). Recordings of earthquake-generated Rayleigh waves traversing the array provide phase velocities in the 12–150 s band. All seismic data were downsampled to 1 Hz sample rate, instrument response removed, and deconvolved to displacement upon download from the EarthScope Data Management Center (array codes ZE, 7B) prior to subsequent processing.

3.1. Tilt and Compliance Correction

For all periods on the vertical component, ocean noise in the form of horizontal and pressure energy (i.e., tilt and compliance) are removed using the Automated Tilt and Compliance Removal package (Janiszewski et al., 2019) based on the formulation of Crawford and Webb (2000). Here we remove tilt and compliance effects from each teleseismic event using transfer functions calculated from the 24 hr prior to the earthquake. In addition, we apply these corrections to daily vertical-component recordings in the 3–10 s band prior to seismic ambient-noise processing, which effectively removes fundamental-mode energy trapped at the water-sediment interface from the resulting correlograms, leaving behind high signal-to-noise ratio (SNR) recordings of first-overtone Rayleigh waves in this short-period band (Adimah et al., 2024; Bowden et al., 2016; Janiszewski & Russell, 2025; Yang et al., 2020).

3.2. Ambient Noise Analysis

We compute ambient-noise empirical Green's functions (EGFs) from cross-correlations of day-long seismograms (Bensen et al., 2007; Russell, Gaherty, et al., 2019; Russell & Gaherty, 2021), utilizing corrected vertical-component and DPG correlations for Rayleigh waves, and transverse components for high-frequency Love-wave (Figure 2). Similar to Russell and Gaherty (2021) we do not perform amplitude (one-bit) normalization of the seismograms prior to correlation, as the unnormalized data produced EGFs with higher SNR in the desired period bands. A SNR threshold >10 is used to select the high-quality EGFs shown in Figure 2.

Phase velocities are extracted from interstation pairs using the approach of Menke and Jin (2015), which fits a zero-order Bessel function (J_0) to the observed cross-spectral amplitude based on Aki's formulation (Aki, 1957). Rayleigh-wave phase velocities are extracted in the 5–10 s period band for the first-higher mode (1S) Rayleigh wave on the vertical component. On the transverse component, fundamental-mode Love waves (0T) in the 5–10 s period band are extracted. Fundamental-mode Rayleigh waves (0S) in the 15–25 s period band are extracted from both the vertical component and DPG correlations; the DPG correlations are particularly useful for improving coverage for stations that experienced seismometer failure (in the 15–25 s period band). Figure 3 provides example fits of Bessel functions fitted to observed spectra for transverse component, vertical component, and DPG in the ambient-noise bands. In all cases, the starting dispersion curves for the fitting process are the array-average dispersion extracted from the linear Radon transforms (Luo et al., 2015) of the correlation functions for each frequency band and associated components (Figure S2 in Supporting Information S1).

3.3. Teleseismic Array Analysis

Rayleigh-wave phase velocities for periods of 12–150 s are measured using the Automated Surface-Wave Measurement System (ASWMS) of Jin and Gaherty (2015), applied to tilt- and compliance-corrected (Janiszewski et al., 2019) vertical-component recordings of teleseismic events with moment magnitudes larger than M_w 5.5 and focal depths shallower than 50 km (Figures 4a and 4c). Earthquakes show excellent back azimuthal coverage (Figures 4b and 4d) for each experiment, with 133 events used for Young ORCA, and 182 events used for Old ORCA (example events shown in Figures 4e and 4f). The ASWMS analysis utilizes a wide band-pass filter applied to each recorded seismogram prior to cross-correlation between nearby stations, followed by narrow-band Gaussian filtering centered on discrete periods where interstation phase is estimated (Jin & Gaherty, 2015). To improve the coherence of the interstation correlations, we follow the approach of Lin et al. (2016) and separated the analysis into three overlapping period bands, with initial wide-band filters applied in short (12–27 s), intermediate (20–100 s), and long (70–150 s) periods bands. Quality control within each band for each

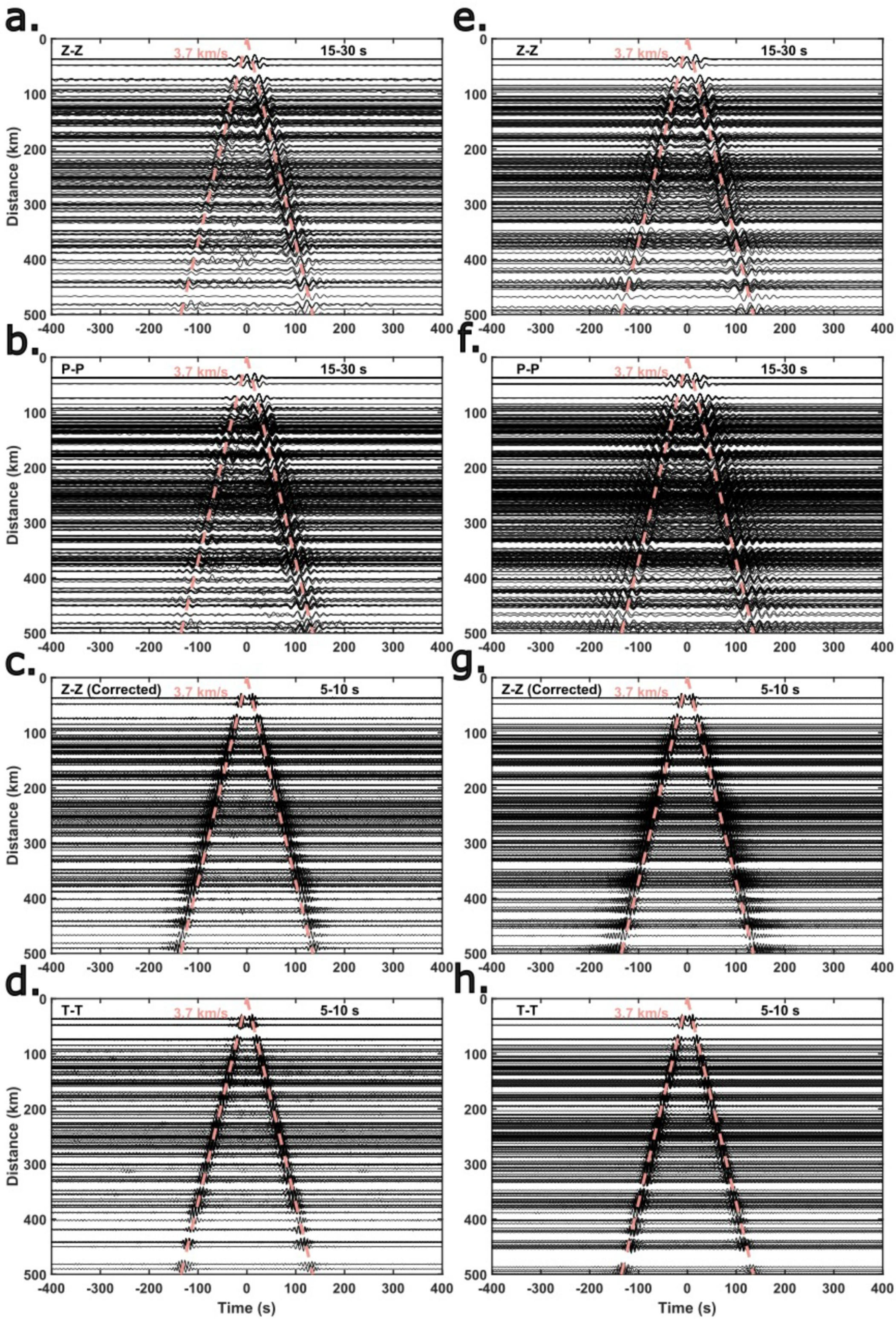
a.
Z-Z
3.7 km/s
15-30 s
b.
P-P
3.7 km/s
15-30 s
c.
Z-Z (Corrected)
3.7 km/s
5-10 s
d.
T-T
3.7 km/s
5-10 s
e.
Z-Z
3.7 km/s
15-30 s
f.
P-P
3.7 km/s
15-30 s
g.
Z-Z (Corrected)
3.7 km/s
5-10 s
h.
T-T
3.7 km/s
5-10 s
Distance (km)
Time (s)

Figure 2.

10.1029/2025JB033545

event requires a minimum Rayleigh-wave SNR > 3, and cross-correlation waveform coherence >0.65. In total, we extracted an average of 61 interstation phase delays per event at each frequency for Young ORCA, and an average of 178 interstation phase delays per event at each frequency for Old ORCA.

3.4. Array-Averaged Phase-Velocity Dispersion and Azimuthal Anisotropy

The collection of ambient-noise inter-station phase velocities and earthquake interstation phase delays are first used to derive "1-D" array-average estimates of phase velocity and its azimuthal variation (anisotropy) at each measured period. For the ambient-noise derived observations, we follow the approach of Russell, Gaherty, et al. (2019) and invert the interstation phase velocities at each period for an isotropic average value, and the amplitude and direction of array-averaged azimuthal variations in phase velocity. For the earthquake-based observations, the phase-delay estimates are inverted for array-average value of mean phase velocity and the amplitude and direction of associated azimuthal variation at each frequency (Lin et al., 2016; Russell, Gaherty, et al., 2019). Azimuthal terms are determined via sinusoidal fit to phase-velocity variations as a function of wave-propagation azimuth (θ), with Rayleigh-wave fits limited to 2θ terms, and Love-wave fits incorporating a combination of 2θ and 4θ terms (Montagner & Nataf, 1986; Russell, Gaherty, et al., 2019). Due to pervasive interference and ambiguity between fundamental and higher-mode Love waves in oceanic regions (e.g., Forsyth, 1975), Love wave observations are limited to very short periods ($T < \sim 8$ s), with the specific upper bound controlled by the shallow lithospheric velocity structure and strength of the low-velocity zone in each region (Figure 3; Russell, Gaherty, et al., 2019). We also discard the fundamental-mode Rayleigh-wave observations dominated by slow Scholte-type waves propagating at the water-sediment interface at periods less than ~16 s.

In detail, both the isotropic phase velocity and the azimuthal variations vary across the arrays. We therefore also invert our observations for two-dimensional variations in phase velocity and azimuthal anisotropy. For the ambient-noise interstation measurements, this inversion uses a finite-frequency approach (Lin & Ritzwoller, 2010; Russell & Gaherty, 2021), while earthquake interstation phase delays are inverted using an Eikonal approach (Lin et al., 2009; Jin & Gaherty, 2015). The results of this analysis are presented in Figure S3 of Supporting Information S1. At shorter periods, both Young and Old ORCA show variations in phase velocity that are suggestive of lithospheric heterogeneity, with variation at Old ORCA (~±3%) much stronger than at Young ORCA (~±1%). At Old ORCA, we find that both the isotropic phase velocities and the direction and strength of azimuthal anisotropy are distinct in the northwest and southeast portions of the array. These variations coincide with a ~200 m step in seafloor depth (and likely ~1 km variation in oceanic crustal thickness), which coincidentally aligns well with the high-density central OBS line that separates the two regions. Cognizant of this change in structure, we separate the Old ORCA observations into two subregions (North and South; Figure S1c in Supporting Information S1) for the 1S period range of 5–10 s and determine array-average phase velocity and anisotropy estimates in each subregion. In contrast, the weak phase-velocity heterogeneity and little variation in strength and direction of azimuthal anisotropy at Young ORCA justifies the use of a single 1D array-average approach. At longer periods (~25 s and longer) at both arrays, observations show only modest variations in phase velocity, consistent with the relatively long wavelength of these observations, the limited aperture of the OBS arrays, and the relatively homogeneous crust and mantle structure within stable oceanic lithosphere.

Figure 5 summarizes the array-average dispersion observations for Young ORCA and both regions of Old ORCA. The short-period observations (both 1S Rayleigh waves and 0T Love waves) are sensitive primarily to the crust and the shallowest mantle lithosphere velocities (Figure S4 in Supporting Information S1), with variations between regions of up to ~2% in both Rayleigh and Love waves that are not straightforward functions of plate age. For the longer-period fundamental mode Rayleigh waves, the phase velocities diverge at periods longer than 20 s in a manner that is consistent with plate cooling, with the Old ORCA observations over 2% faster than the Young ORCA observations at periods most sensitive to the thickening thermal boundary layer (~20–50 s). The velocity

Figure 2. Bandpass filtered ambient noise cross-correlation functions (CCFs) for Young ORCA (a–d) and Old ORCA (e–h). (a) Vertical component showing fundamental-mode Rayleigh wave (0S) in the 15–30 s band. (b) Pressure component capturing Rayleigh fundamental mode (0S) in the 15–30 s band; (c) Vertical component with tilt and compliance removed prior to calculation, revealing first higher-mode Rayleigh waves (1S) in the 5–10 s band; and (d) transverse component highlighting the Love wave (predominantly fundamental mode, 0T) in the 5–10 s band. In panels (e–h) Same as (a–d), but for Old ORCA. A group velocity of 3.7 km/s is marked by the peach dashed line ($\mathrm{SNR} = \frac{\mathrm{RMS\ (signal)}^2}{\mathrm{RMS\ (noise)}^2}$, where *signal* is any arrival with group velocity >1.5 km s^{-1} and *noise* is <1.5 km s^{-1}).

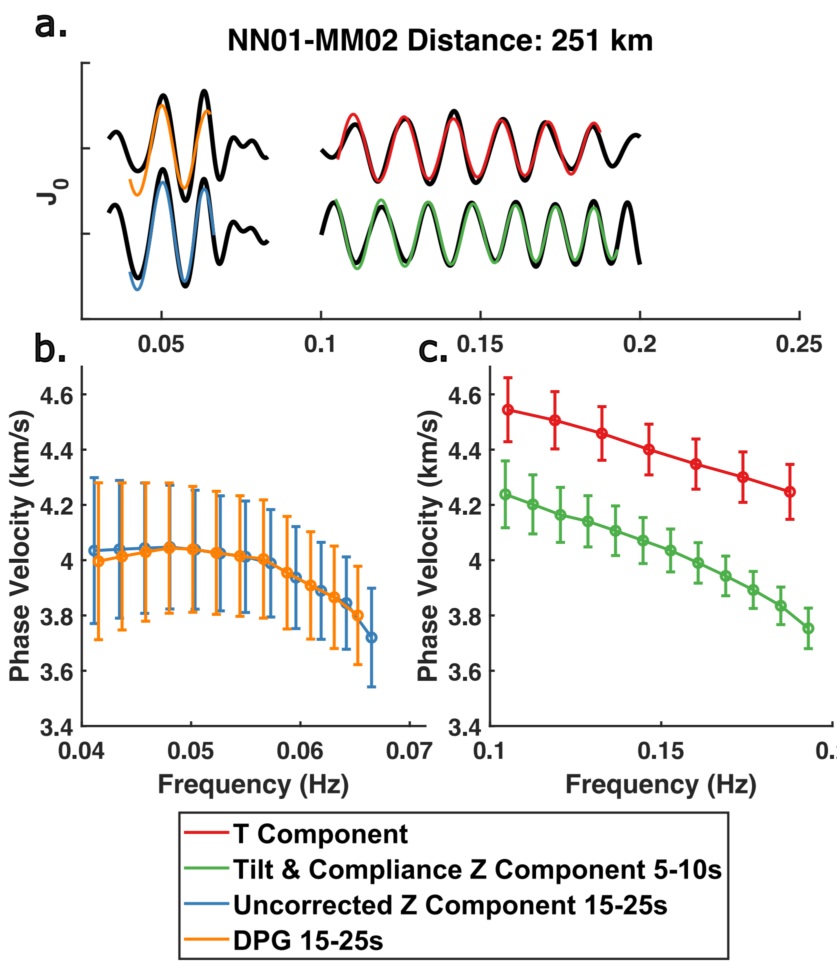

Figure 3. Bessel function fitting procedure to extract interstation phase velocities from ambient noise at Old ORCA using the method of Menke and Jin (2015). (a) Contains the observed real part of the cross-spectra in black for DPG, corrected first-overtone Z, uncorrected Z, and T components. Colored lines indicate the zero-order Bessel function J_0 fit to the spectra for DPG in orange (15–25 s), uncorrected Z in blue (15–25 s), T component (5–10 s) in red, and corrected Z (5–10 s) in green. (b) The extracted phase velocity for longer period DPG and uncorrected Z, with colors indicated in top panel. (c) Same as left panel, for the corrected Z and T components.

difference persists but gradually diminishes as period increases. These observations will provide the basis for regional one-dimensional radially anisotropic reference models that provide the framework for evaluating azimuthal anisotropy variations.

Azimuthal variation in phase velocity with respect to the 1D averages are presented in Figures S5 and S6 of Supporting Information S1, and the 2θ and 4θ fits to these variations are summarized in Figure 6 (Love azimuthal variation in Figure S7 of Supporting Information S1). Several characteristics of oceanic mantle anisotropy are apparent from these observations. Rayleigh waves show significant variations in the strength and orientation of azimuthal anisotropy as a function of period in all regions, suggesting significant depth variability in the underlying anisotropic fabric. We also observe major differences in Rayleigh-wave anisotropy strength and orientation between regions, with stronger anisotropy observed in the Young ORCA region than either of the Old ORCA regions. At periods associated with lithospheric depths (5–20 s), the strength of Rayleigh anisotropy at Young ORCA ranges from ~2%–3% (Figure 1a), while at Old ORCA it ranges from 1% to 2%, with the south Old ORCA region particularly weak at ~1% (Figure 6c). In addition, while the short-period observations at Young ORCA have a direction that appears largely consistent with the inferred FSD (Figure 6b), both Old ORCA regions have anisotropic orientations that are rotated by 15–40° from FSD (Figure 1d). At longer periods dominated by asthenospheric fabric, Young ORCA anisotropy persists with a strength of ~2.5%–3% before decaying at the longest periods, and the apparent orientation rotates toward a value consistent with local apparent plate motion

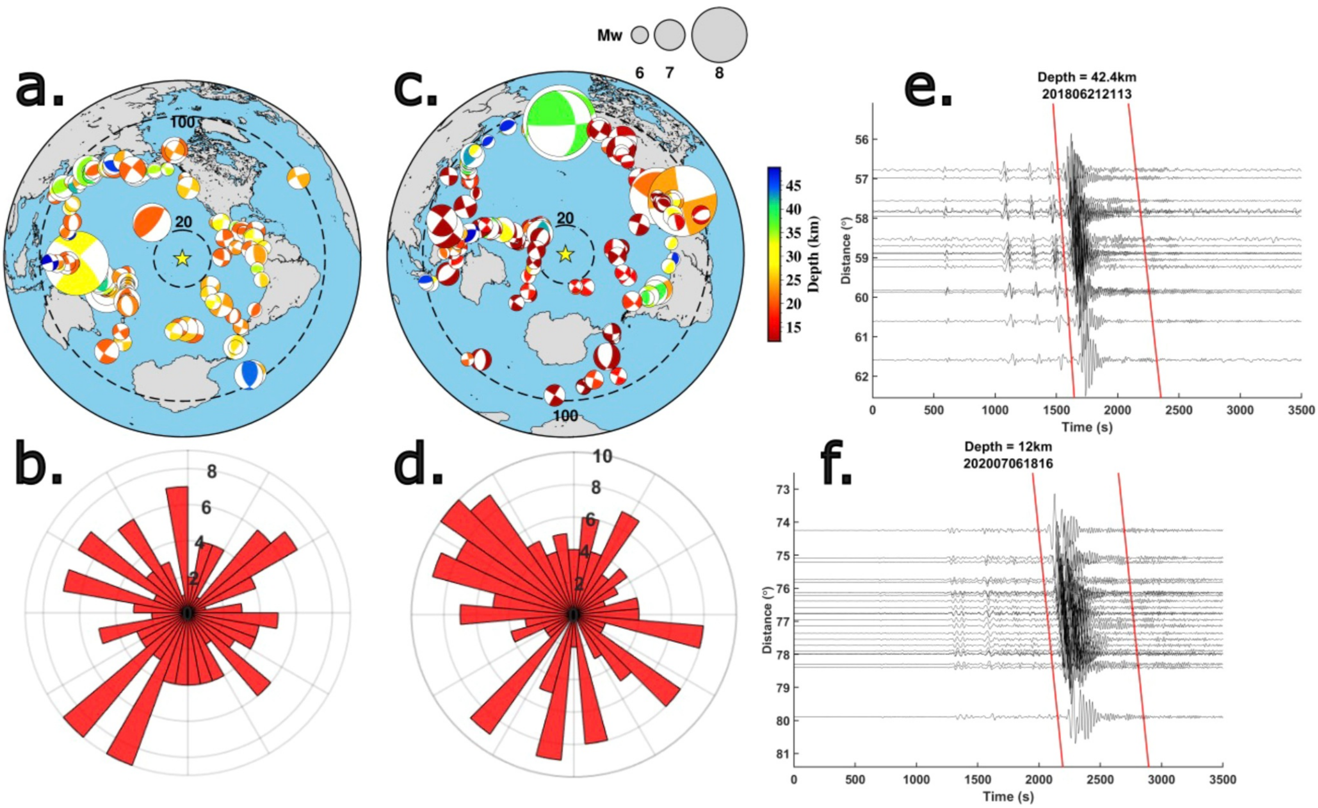

Figure 4. Distribution of vertical component M_w 5.5 and greater earthquakes that pass quality control, filtered in the 20–100 s band, and are used in the ASWMS analysis. (a, b) Young ORCA earthquake focal mechanisms (b) and rose diagram of azimuthal distribution (a) of earthquakes relative to array location. In panels (c, d) Same as (a, b) for Old ORCA. (e, f) Example earthquakes with red lines indicating windows around surface waves for (e) Old ORCA M_w 6.2 at 12 km depth on 2,020/07/06 at 18:16 and (f) Young ORCA M_w 6.2 at 42.4 km depth on 2018/06/21 at 21:13.

(APM) at ~80–100 s period and continues beyond APM at longer periods. Old ORCA displays much more heterogenous behavior, remaining quite weak (~1%) in the 20–60 s band, increasing to ~2.5% at a period of 70 s, and then decaying with increasing period, similar to Young ORCA. The Old ORCA fast directions in the 20–60 s period range rapidly transition from the lithospheric values noted above to a direction that appears largely consistent with APM, before rotating back away, clockwise, at the largest periods.

Love wave azimuthal anisotropy (Figures S5–S7 in Supporting Information S1) is estimated in a limited period band, with higher degrees of uncertainty than the Rayleigh observations. In all regions, both 2θ and 4θ variability is measurable with estimated amplitudes of 1%–2%. These variations have smaller errors and are visually more coherent for Young ORCA, despite higher horizontal component noise, whereas for Old ORCA they are less well resolved, with greater scatter apparent in the observations and correspondingly large errors, even though horizontal component noise is lower (Figures S6 and S7 in Supporting Information S1). The 4θ variations are expected for orthorhombic fabrics associated with olivine deformation in the mantle, with a fast direction i.e. rotated ~45° from the Rayleigh-wave fast direction observed at comparable periods, but rarely have been observed directly (e.g., Russell, Gaherty, et al., 2019). The 2θ Love-wave variations are generally expected to be very weak and rotated ~90° from Rayleigh-wave fast direction (Montagner & Nataf, 1986; Russell, Gaherty, et al., 2019). For Young ORCA, the direction of the 4θ component is rotated ~45° from the observed Rayleigh-wave fast direction at similar periods, consistent with the expected relationship for typical mantle fabrics (e.g., Russell, Gaherty, et al., 2019). For Old ORCA, the directions do not conform to the expected 45° offset, perhaps because they are less robustly estimated. The 2θ Love-wave anisotropy is stronger than expected for olivine fabrics (similar to Russell, Gaherty, et al. [2019]), and is generally rotated from the expected direction at both arrays. This anomalous 2θ anisotropy may demonstrate Rayleigh-Love coupling on a dipping symmetry axis (Liu & Ritzwoller, 2025).

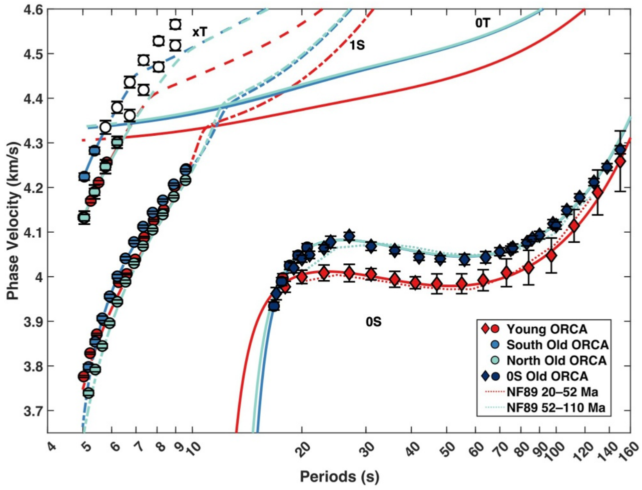

Figure 5. Rayleigh and Love phase velocity dispersion for Young and Old ORCA. Symbols and lines shown in red correspond to Young ORCA, while blue shades correspond to Old ORCA. Measurements derived from ambient noise are shown with circles, while teleseismic earthquake observations are shown with diamonds, and error bars represent one standard error of the mean. Measurements for fundamental-mode Rayleigh waves (0S), Love waves (0T), and first-overtone Rayleigh waves (1S) are labeled. The higher-frequency (5–10 s 1S and 0T) observations at Old ORCA have been split into two subregions (North and South) as described in the text, and are indicated by lighter blue and darker blue shading, respectively. For each set of observations, the predicted phase velocities from our final median best-fitting model are shown as solid (fundamental mode) or dashed (first overtone) curves in the same color. The calculated fundamental and first-overtone Love-wave phase velocity curves kiss at 5–6 s period for all three regions, and the observations beyond this cross-over point (open circles) are discarded due to ambiguity in their interpretation. For reference, the predicted fundamental-mode Rayleigh wave phase-velocity from two age ranges of Nishimura and Forsyth (1989) (NF89 20–52 Ma; NF89 52–110 Ma) are shown as dotted lines.

4. Azimuthally Anisotropic Shear Velocity Inversion

Young and Old ORCA array-average isotropic phase velocities and anisotropy are inverted for depth dependent shear velocity, radial anisotropy, and azimuthal anisotropy in two steps, following Russell, Gaherty, et al. (2019). For Young ORCA, we present a single 1D model that represents anisotropic shear-velocity structure averaged over the entire array footprint. For Old ORCA, we present two 1D models above 65 km depth and a single average model below 65 km, allowing us to incorporate the distinct north and south sub-array averages observed in the short-period (5–10 s) data. The general procedure and scaling assumptions are outlined here.

First, isotropic Rayleigh (5–150 s) and Love wave (5–7.5 s) phase velocities are jointly inverted for the transversely isotropic (TI) structure from the surface to 400 km depth. We solve for V_{SV} (velocity of horizontally propagating vertically polarized shear waves) and V_{SH} (velocity of horizontally propagating horizontally polarized shear waves) in the crust and upper ~65 km of the mantle, providing an estimate of radial anisotropy, $\xi = \left(\frac{V_{SH}}{V_{SV}}\right)^2$ in the crust and shallow mantle lithosphere. Deeper than ~65 km, V_{SH} is increasingly damped toward V_{SV}, assuring $\xi = 1$ (radial isotropy) beneath 65 km depth. Sensitivity kernels representative of the full range of frequencies are presented in Figure S4 of Supporting Information S1. The Voigt averaged model from the NoMelt array (Lin et al., 2016; Russell, Gaherty, et al., 2019) is used as the starting model from which these kernels are computed. For Young ORCA, we alter this starting model only by adjusting the water depth to an array average of 4,625 m while fixing sediment thickness to 150 m, equivalent to NoMelt. For Old ORCA, we find that assuming a constant NoMelt crustal structure fails to fit first-overtone Rayleigh wave observations comparably well in the north and south regions. As noted previously, the offset in bathymetry and associated Bouguer anomaly (Figure S1 in Supporting Information S1) variations are suggestive of slightly thicker crust in the NW relative to the SE. For both the north and south regions, we undertake a preliminary set of phase-velocity inversions by grid searching through a range of thicknesses (5.8–7.0 km) of oceanic crust (Figure S8 in Supporting Information S1) to determine the crustal thickness that best fits the observations in each region. On the basis of this test, we use crustal thicknesses of 6.7 km in the north region and 5.9 km in the south region. For the radial anisotropy inversions, we enforce layers of constant ξ in the lower crust and mantle, respectively, due to poor depth sensitivity of the 5–7.5 s Love waves to V_{SH} (Russell, Gaherty, et al., 2019); ξ is forced to decrease linearly to 1 (isotropic) between the top of the lower crust and the sediment-basement interface. Compressional velocities V_{PV} and V_{PH} and their ratio $\phi = \left(\frac{V_{PV}}{V_{PH}}\right)^2$ are scaled from V_{SV} and V_{SH} by preserving the starting model's Voigt average $\frac{V_P}{V_S}$ (~1.78–1.84 km/s) and enforcing $\phi^{-1} = \xi$ (Brunsvik & Eilon, 2023; Montagner & Anderson, 1989). The radial anisotropy parameter η is held to PREM values (Russell, Gaherty, et al., 2019). Below 300 km depth the model is damped toward oceanic model PA5 (Gaherty et al., 1996) and not interpreted. We apply the aforementioned constraints within an iterative linearized least-squares inversion following Russell, Gaherty, et al. (2019). The inversion is regularized using a second-derivative smoothing constraint to limit model variability with depth and norm damping toward the starting model to improve stability at each iteration with a stable solution found after 8 iterations. Forward calculation of phase velocity and associated perturbation kernels employ the MINEOS normal-mode based code. Physical dispersion effects due to seismic attenuation are applied to the mode eigenfrequencies assuming the Q_μ structure of Ma et al. (2020) and a reference frequency of 35 mHz. We estimate uncertainties for V_{SV} and V_{SH} via 500 bootstrap iterations. For each iteration, we invert surface-wave dispersion data randomly selected from a Gaussian distribution with mean values equal to the original data and standard deviation defined by their 1-σ uncertainties. The median, middle 68th, and 95th percentiles of the

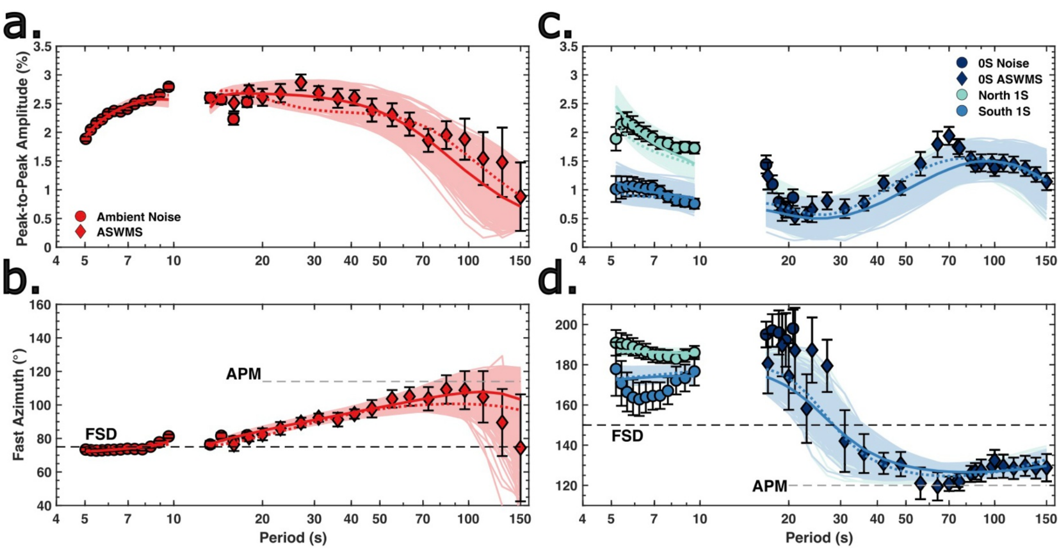

Figure 6. Rayleigh wave azimuthal variations in phase velocity for the ORCA arrays. (a, b) Young ORCA azimuthal anisotropy measurements for Rayleigh wave peak-to-peak amplitude (a) and fast azimuth (b) Light colored lines show bootstrap model predictions, and the thick line shows the median model prediction. The median layered model predictions are shown by the dashed lines. The black dashed line indicates fossil-spreading direction (FSD) and gray dashed line absolute plate motion (APM). In panels (c, d) Same as (a, b) for Old ORCA including north and south first-overtone measurements for each region of Old ORCA, and common 0S observations for the entire array.

resulting model ensemble with acceptable misfit $\left(\chi^2 \leq 2\right)$ are taken as the final model and 1-σ or 2-σ uncertainties, respectively.

Second, azimuthal anisotropy measurements of Rayleigh (5–150 s) and Love waves (5–7 s) are inverted for the strength and orientation of azimuthal anisotropy parameters G and E following Montagner and Nataf (1986), using a single-step inversion and perturbation kernels calculated from the TI model with the same radial knot structure (Figure S9 in Supporting Information S1). Parameters $|G|$ and ψ_G describe the strength and fast azimuth of V_{SV} anisotropy, respectively, and we invert for these values through the crust at Old ORCA (see Section 5.2) and from the Moho at Young ORCA, then down to 400 km based on the strength and azimuth of 2θ azimuthal variations of Rayleigh and Love waves. Parameters $|E|$ and ψ_E correspond to the strength and fast direction of V_{SH} anisotropy, and are inverted for only in the upper 25 km, from the 4θ azimuthal dependence of Love waves (Russell, Gaherty, et al., 2019). Additional anisotropic parameters B and H, which correspond to azimuthal variations of V_{PH} and η, respectively (Montagner & Nataf, 1986) can also weakly contribute to the azimuthal variations of Rayleigh waves. Guided by observations from mantle peridotites (e.g., Ben Ismaïl & Mainprice, 1998; Peselnick & Nicolas, 1978), we scale these parameters to $|G|$ and ψ_G using the approach of Russell, Gaherty, et al. (2019). In all cases, the anisotropic terms within the inversion are parameterized by the amplitudes of the cosine and sine components of each term (Russell, Gaherty, et al., 2019) with second-derivative smoothing with depth, which are then converted to the more intuitive anisotropic strength ($|G|$ or $|E|$) and relative fast azimuth (ψ_G and ψ_E). The final values and associated uncertainties for all azimuthal anisotropy parameters are estimated via the same bootstrapping procedure described above for the radial anisotropy, resampling over 1,000 iterations. For $|G|$ and ψ_G, our preferred parameterization employs smooth variations with depth to characterize the cosine and sine coefficients, and in turn, anisotropic strength and direction. However, given that abrupt changes in anisotropy are possible at locations such as the lithosphere-asthenosphere boundary, we also explore layered parameterizations that allow sharp transitions in anisotropy to guide our interpretation. The layered parameterization introduces discontinuous breaks at 50 and 200 km depth for Young ORCA, and 70 and 200 km depth for Old ORCA, with the same smoothly varying parameterization above, between, and below these discontinuities. Significant changes in $|G|$ and ψ_G across the discontinuities are not enforced or encouraged; they are simply enabled by breaking the model smoothness constraints at the specific depth nodes associated with the discontinuity. This approach allows for abrupt changes in anisotropy between with the lithosphere, the sub-lithospheric asthenosphere, and deeper upper mantle, respectively, if such changes are desired by the data.

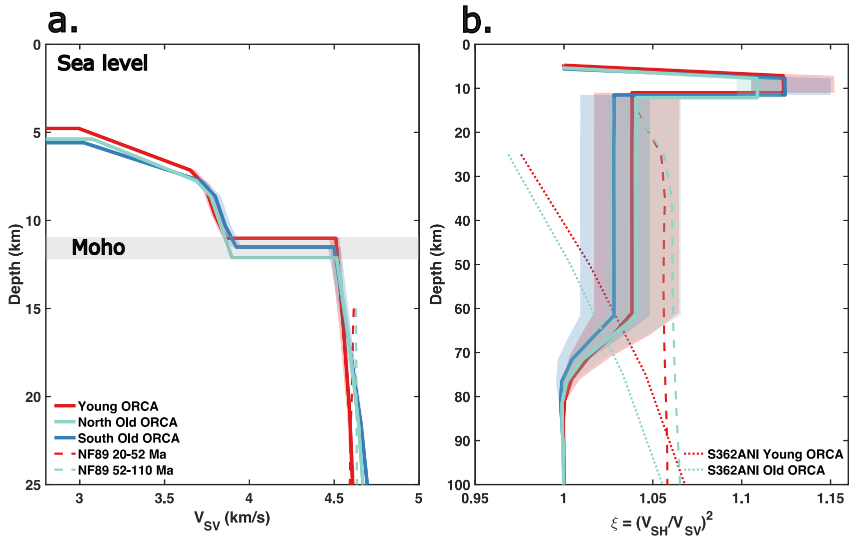

Figure 7. Inversion results for V_{SV} and radial anisotropy $\xi = \left(\frac{V_{SH}}{V_{SV}}\right)^2$ for ORCA arrays. (a) V_{SV} to 25 km depth, crust and uppermost mantle depths. Solid lines are V_{SV} 1-D profiles Young ORCA (red), north and south subregions of Old ORCA (blues), with 2-σ shaded bounds (difficult to distinguish in the crust and uppermost mantle because uncertainties are narrow due to regularization toward the starting model). Dashed lines are representative age regions of Nishimura and Forsyth (1989) (NF89) and dotted lines are from the S362ANI model of Kustowski et al. (2008). (b) Radial anisotropy, ξ, to 100 km depth with the same bootstrap uncertainties as (a).

The depth of the shallower break is chosen based on the approximate thermal lithospheric thickness inferred from the V_{SV} profile in each region, and the deeper break is chosen to approximate the base of the low-Q asthenospheric channel inferred in both regions (Russell et al., 2024). For reference, the shallow discontinuity depths (50, 70 km) agree to within 5 km with the predictions for the 1,100°C isotherm for ~40 and ~90 Ma plate ages, assuming a plate cooling model with 1,350°C potential temperature, 125 km plate thickness, and temperature-dependent thermal conductivity. Misfit tests produce similar anisotropy results for shallow discontinuity choices of 30–50 km for Young ORCA, and 70–90 km for Old ORCA (Figure S13 in Supporting Information S1). In both regions, the layered and smooth parameterizations provide similar fits to the surface-wave data, as discussed below.

5. Results

5.1. Radial Anisotropy and Shear Velocity

Array-average vertical profiles of shear velocity (V_{SV}) and radial anisotropy (ξ) for the Young and both Old ORCA regions are shown in Figures 7 and 8. Crustal V_{SV} values in all three models are characteristic of canonical oceanic crust (Christeson et al., 2019), with a thin (~2 km), high-gradient upper crust overlying a ~4-km-thick lower crust with nearly constant V_{SV} value of 3.77–3.85 km/s (Figure 7). The thickness of the basaltic crust varies slightly between the three models: 5.9 km at south Old ORCA (the starting value of the NoMelt reference model), 6.2 km at Young ORCA, and 6.7 km at north Old ORCA. Radial anisotropy in the crust is found to be non-zero and positive ($V_{SH} > V_{SV}$), with values of ξ that range from 1.10 to 1.14, similar to that observed in the NoMelt region (Russell, Gaherty, et al., 2019). The radial anisotropy in the shallow lithospheric mantle is required to be positive with values of 1.03–1.05, similar to NoMelt and significantly more positive (even of opposite sign) than that found for these regions in some global and Pacific-basin models (Figure 7; Russell, Gaherty, et al., 2019).

Figure 8 displays V_{SV} profiles for Young and Old ORCA regions through the upper 300 km of the mantle. All models display the characteristic signature of oceanic upper mantle: a high-velocity oceanic lid with velocities generally >4.5 km/s; a distinct low-velocity zone near 100–125 km depth with minimum velocities as low as 4.2 km/s; and a region of increasing velocity extending from ~150-km depth to the base of the model (300 km depth) at least. The velocity and apparent thickness of the fast lithospheric lid are larger for Old ORCA (4.4–4.7 km/s, ~75 km) than Young ORCA (4.4–4.6 km/s, ~50 km), generally consistent with oceanic plate

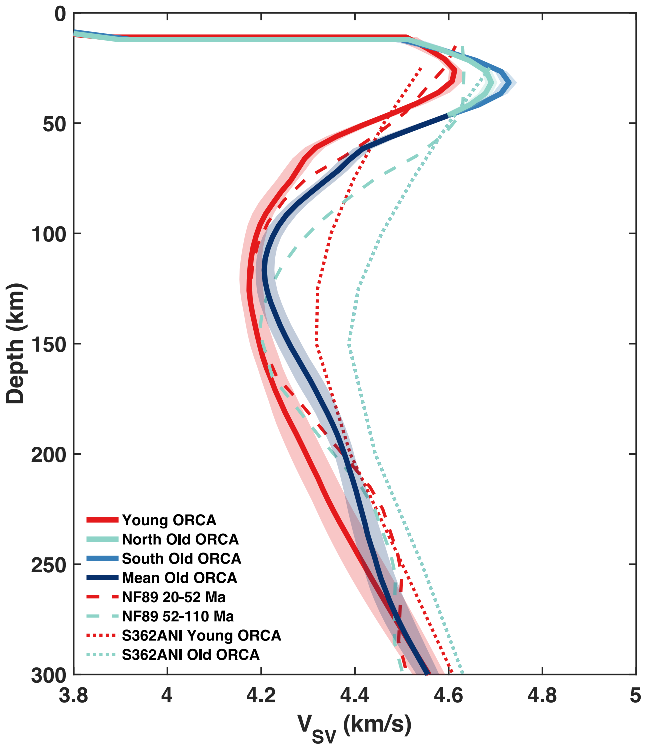

Figure 8. Inversion results for V_{SV} spanning the lithosphere-asthenosphere system (0–300 km depth) beneath the ORCA arrays. (a) Solid lines are V_{SV} 1-D profiles, Young ORCA (red), north and south subregions of Old ORCA (blues) with 2-σ shaded bounds. Dashed lines are representative age regions of Nishimura and Forsyth (1989) (NF89) and dotted lines are from the S362ANI model of Kustowski et al. (2008).

cooling and thickening with age. An unusual feature of the lithospheric structure is the strong positive velocity gradient in the shallowest mantle, with the peak in velocity occurring within the mid-lithosphere (~30 km depth) in all regions. This strong positive velocity gradient is unexpected for typical peridotite-based mantle lithologies, which should have a modest negative velocity gradient due to the rapidly increasing temperature in the lithospheric thermal boundary layer (Lizarralde et al., 2004; Stixrude & Lithgow-Bertelloni, 2012). However, inversion tests suggest that it is required by our observations (Figure S10 in Supporting Information S1). Within the low-velocity zone, the velocity lacks an age dependence, with minimum value of ~4.2 km/s observed at both Young and Old ORCA. This velocity appears to be significantly (~0.1 km/s) lower than the asthenospheric velocity estimated from a nearly identical modeling effort in the NoMelt region (Russell, Gaherty, et al., 2019). Detailed analyses of ORCA isotropic velocity variations in terms of thermal and compositional state of the lithosphere and asthenosphere are a topic of other studies (Phillips et al., 2024; Russell et al., 2024); here we mainly utilize these profiles to guide our interpretation of accompanying anisotropy observations.

5.2. Azimuthal Anisotropy

Figure 9 presents the array-average profiles of V_{SV} azimuthal anisotropy $|G|$ and ψ_G for Young and both Old ORCA regions. The profiles exhibit considerable variations between regions in both the strength and direction of azimuthal anisotropy within the upper 300 km, spanning crust and mantle. At depths associated with the mantle lithosphere (<75 km), $|G|$ anisotropy is quite strong (Figure 9a) in the Young ORCA region (~3.0 ± 0.2%), but is notably weak in both subregions of Old ORCA, with values that range from ~0.5% to a maximum of ~2.0 ± 0.2%. The azimuthal anisotropy appears to extend into the crust in Old ORCA (Figure S11 in Supporting

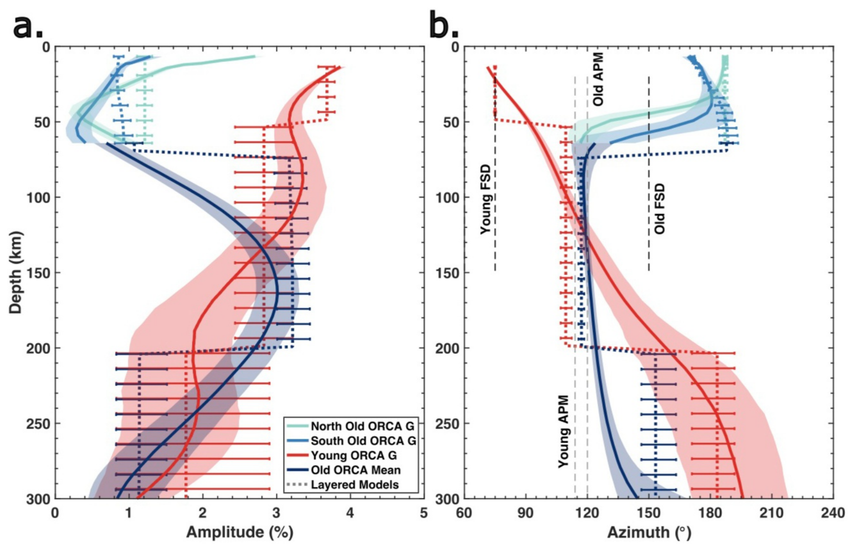

Figure 9. Azimuthal anisotropy profiles, showing $\left(\frac{G}{L}\right)$ amplitude (a) and fast azimuth (b) for the smooth (solid) and layered (dotted) inversion parameterizations. Red profile shows Young ORCA result and blue profiles correspond to the Old ORCA north and south subregion results with darker blue the mean of subregion profiles below 65 km. Shaded regions are the 1-σ bootstrap uncertainties for the smooth model and whiskers spaced every 10 km are 1-σ uncertainties for the layered model. Dashed black and gray lines are fossil spreading direction (FSD) and absolute plate motion (APM), respectively, for each respective array.

Information S1), a characteristic that is not required by the data at Young ORCA. The lithospheric $|G|$ anisotropy beneath the southern portion of Old ORCA is modestly weaker than the northern region, clearest in the upper lithosphere (above ∼30 km depth). These amplitude differences are robust regardless of whether we use a smooth or layered parameterization for the anisotropy. However, for the Old ORCA regions, the detailed structure of the strength of lithospheric anisotropy depends on model parameterization. Smooth models show a strong negative gradient of anisotropy with depth: in the north ∼2 ± 0.2% in the crust and shallowest mantle declines to effectively 0% at ∼70 km depth, while in the southern region it decreases from ∼1 ± 0.2% in the crust and shallow mantle to 0% at ∼70 km depth. In both Old ORCA sub-regions (which are not separable deeper than the plate), anisotropy strength increases from 70 km to much higher values (∼3%) in the asthenosphere. When using a parameterization that allows for a discontinuity in anisotropy at ∼70 km depth, this strong gradient in strength within the lithosphere largely disappears, with the northern region showing a nearly constant value of anisotropy at ∼1.5%, and the southern region moderately increasing in strength from ∼1% at shallow depth to ∼1.2% at 70 km depth.

At asthenospheric depths, the strength of anisotropy is similar between regions (Figure 9a). Beneath Young ORCA, relatively strong (∼3.0 ± 0.5%) anisotropy continues from the lithosphere to a depth of 125–150 km before decreasing to more modest values of ∼2 ± 1% below 200 km depth. Beneath Old ORCA, the average model at asthenospheric depth is again dependent on parameterization (similar to Young ORCA), but for both smooth and layered parameterization, it is overall similar to Young ORCA—relatively strong $|G|$ (∼3.0 ± 0.5%) anisotropy in the 100–200 km depth range, and weaker anisotropy deeper. This regional similarity is much more apparent for the layered parameterizations, in which both Young and Old ORCA display nearly constant values of anisotropy of 2.5%–3.5% in the 70–200 km depth range, overlying a deeper zone with 1.5%–2% anisotropy. In the smooth parameterization for Old ORCA, the unusually weak lithospheric anisotropy results in the need for a rapid increase in strength (∼3% over an ∼80 km depth range) through the uppermost asthenosphere, resulting in models that have a peak in $|G|$ anisotropy at 150–200 km depth, which is deeper than that of Young ORCA (∼70–110 km).

The orientation of ψ_G, which provides the fast azimuth of V_{SV}, also varies strongly between regions (Figure 9b). To evaluate these variations, we compare the modeled fast azimuths with the expected values for the commonly hypothesized controls on anisotropic fabric, namely fossil spreading direction (FSD) in oceanic lithosphere, and absolute plate motion (APM) in the asthenosphere. In the lithosphere, Young ORCA is characterized by a ψ_G (75 ± 5°) that corresponds closely to the FSD azimuth of 78° within the upper 10–20 km of the mantle, but it then rotates in a clockwise direction significantly from FSD at depths that still correspond to the high-velocity lithosphere (20–60 km; Figure 8). This rotation does not appear in the layered parameterization, which instead displays a nearly constant ψ_G that agrees very closely with FSD throughout the lithosphere. However, the fit of the observed strength of anisotropy in the period range sensitive to the deeper lithosphere (25–50 s) is degraded for the layered model (Figure 6a), implying that the smooth variation may be preferred by the data. At both Old ORCA regions, the lithospheric fast direction is significantly rotated ∼15°–45° clockwise relative to the estimated FSD azimuth of 150°, although as discussed above, the fabric is fairly weak in much of the Old ORCA plate. In the southern region, the fast direction in the crust and shallowest mantle systematically increases across the lithosphere, from values of 165 ± 5° in the crust and shallowest mantle, to 195 ± 15° at the plate's inferred base. In the northern region, the fast direction appears less variable and ranges in value from 185 ± 5° just below the seafloor to 195 ± 15° at 70 km depth. These inferred directions and their variation with depth are very similar for both the smooth and layered parameterizations.

At asthenospheric depths, below ∼70 km depth, the fast azimuth observed at Old ORCA rotates counterclockwise over an exceptionally narrow (∼20 km) depth range to 120 ± 10° (Figure 9b). 120° matches almost exactly with the direction of APM here, and this agreement persists to a depth of at least 200 km, where the fast direction rotates slightly clockwise with increasing depth. The smooth and layered parameterization models are very similar across this entire depth range. For Young ORCA at asthenospheric depths (below ∼50 km), the smooth inversion results in models with a ψ_G that smoothly rotates from approximately EW to a value (120 ± 10°) consistent with regional APM at ∼125 km depth, before continuing to rotate to values of 170–210° in the deeper upper mantle. The layered parameterization significantly breaks up this smooth variation, resulting in an asthenospheric layer from 60 to 200 km with fast direction (110 ± 10°) roughly consistent with regional APM, and a deep layer below 170 km depth with fast direction of approximately 200 ± 30°.

10.1029/2025JB033545

The seismic parameter E, which describes the strength and azimuthal alignment of 4θ variability of V_{SH}, is estimated from the Moho to ∼50 km depth (Figure S12 in Supporting Information S1). Due to the limited frequency range of Love-wave observations, we do not attempt to resolve depth dependence of E. At Young ORCA, ψ_E has a value of 115 ± 5°, which is rotated by ∼40° from ψ_G and thus roughly consistent with olivine-based fabrics (for which we would expect them to differ by 45°). The Young ORCA $|E|$ amplitude is 3.1% ± 0.5%, stronger than previously observed at NoMelt (∼2.5%; Russell, Gaherty, et al., 2019). At Old ORCA, ψ_E has a value of 225 ± 5° (north) and 193 ± 5° (south), with corresponding amplitudes $|E|$ of 0.6% ± 0.2% (north) and 1.4% ± 0.3% (south). The north subregion direction is roughly consistent with expected value based on ψ_G, but the south subregion is not. In addition, the relative amplitude of the Old ORCA $|E|$ values (weaker in the north, stronger in the south) are flipped relative to $|G|$. We infer that these scattered and somewhat contradictory estimates of $|E|$ are the product of: (a) the relatively weak upper-lithosphere anisotropy in the Old ORCA region, which produces 4θ Love-wave variations that are at the resolution limit of our azimuthal sampling and/or (b) the strong depth-dependent gradients in anisotropic fast direction in the shallow lithosphere, as evidenced by ψ_G, which would be more likely to obscure a 4θ signal.

6. Discussion

The set of ORCA models add to the growing collection of regional-scale OBS-based constraints on the oceanic lithosphere-asthenosphere system (e.g., Eilon & Forsyth, 2020; Kawano et al., 2023; Laske et al., 2026; Lin et al., 2016; Mazzullo et al., 2017; Rychert & Harmon, 2017; Saikia et al., 2021; Takeo et al., 2014, 2016, 2018). Prior to these contributions, the geodynamic behavior of this system, as constrained by seismic anisotropy, was largely derived from global and ocean-basin-scale anisotropic tomography models of the large-scale distribution of anisotropy (in particular the strength and direction of V_{SV} anisotropy parameter $|G|$ and ψ_G, respectively) (e.g., Beghein et al., 2014; Burgos et al., 2014; Debayle & Ricard, 2012, 2013; Debayle et al., 2016; Eddy et al., 2022; Montagner & Tanimoto, 1991; Montagner, 2002; Schaeffer et al., 2016; Yuan & Beghein, 2018) Coupled with geodynamic calculations capable of modeling flow and associated fabric development in the asthenosphere (e.g., Becker et al., 2014; Conrad & Behn, 2010; Fraters & Billen, 2021), these seismic models suggest that anisotropic fast directions correlate with APM, and are likely driven by shear in the asthenosphere at the interface between the overriding plate and the underlying mantle. This correlation clearly does not hold everywhere, however (e.g., Becker et al., 2014), and these models also are less successful at characterizing lithospheric fabric hypothesized to arise due to spreading-parallel corner flow during seafloor spreading (e.g., Gaherty et al., 2004; Hess, 1964; Mark et al., 2019; Nishimura & Forsyth, 1989), presumably due to inability to resolve abrupt small-scale changes in spreading direction (Becker et al., 2014; Nishimura & Forsyth, 1989) and/or the limited resolution at shallow depths of the long-period surface waves used in those studies. Here we explore the implications of our new regional anisotropy models for our understanding of the oceanic lithosphere-asthenosphere system.

6.1. Asthenospheric Fabric: Multi-Scale Flow and Deformation Beneath Oceanic Plates

Observations of seismic anisotropy in the convecting asthenosphere capture the interplay between internal deformation processes with a variety of scales, including lateral pressure-driven flow (e.g., Nagel et al., 2008; Semple & Lenardic, 2018) and buoyancy-driven convection (e.g., Ballmer et al., 2007), all sheared from above by plate motion. The relative strength and direction of observed anisotropy will depend on the depth distribution of the shear deformation associated with that flow, as well as the rate, direction, and volumetric extent of deeper or intra-asthenospheric flow fields relative to plate motion (e.g., Silver & Holt, 2002; Wang et al., 2025). An observation that anisotropy direction correlates with APM suggests either that internal, small-scale asthenospheric convection rates are relatively slow (small compared to rate of plate motion), that strain is small or inconsistently aligned (e.g., Boneh et al., 2015; Kaminski & Ribe, 2002), or that convection is disorganized over the observing length scale such that the only coherent component is that associated with plate motion (as inferred from large-scale models). Deviations from APM imply that the internal asthenospheric flow velocities are comparable to or greater than those associated with plate-driven flow, in a direction distinct from APM.

As above, the development of observable anisotropic fabric depends not just on flow velocity, but also on the magnitude of finite strain, the volume of deforming material compared to seismic wavelengths, the deformation history, and the operative creep mechanism. Here, we consider the characteristics of asthenosphere deformation suggested by the ORCA models, in conjunction with similarly derived models from the ∼70-Ma NoMelt region

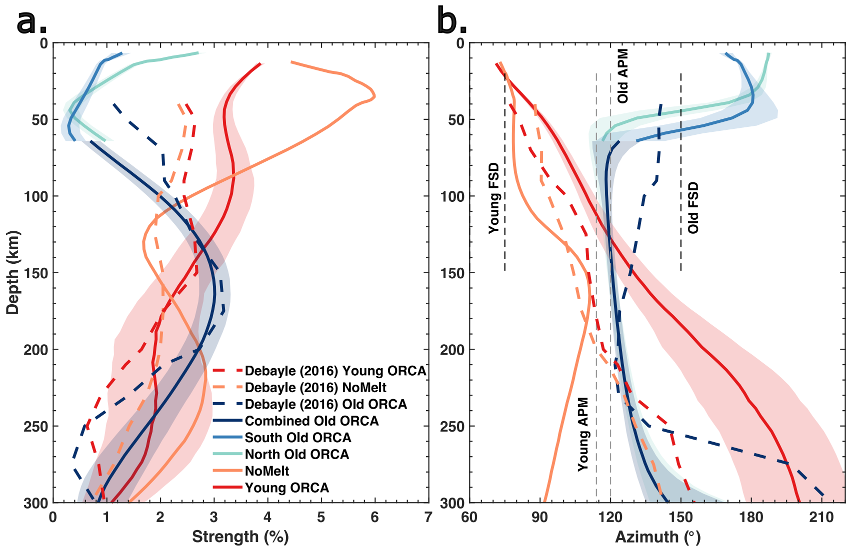

Figure 10. Azimuthal anisotropy (a) strength and (b) azimuth results of this study (Figure 9) in solid lines and shaded uncertainties as previously stated, compared to the azimuthally anisotropic model of Debayle et al. (2016) in dashed lines (current model as of 2022 from IRIS DMC (Trabant et al., 2012)) and NoMelt model (Lin et al., 2016; Russell, Gaherty, et al., 2019).

(Russell, Gaherty, et al., 2019). In this discussion, we take into account the rheological and dynamic character of the asthenosphere in all three regions, as derived from isotropic shear velocity and attenuation modeling (Russell et al., 2024) and body-wave tomography (Eilon et al., 2022; Hariharan et al., 2025). These studies suggest that the ORCA regions are characterized by a highly attenuating (low Q), low-velocity, narrow (~100-km thick) asthenospheric channel with relatively low viscosity, while the NoMelt region has significantly lower attenuation and higher velocity within a broader asthenosphere that suggests higher viscosity (Ma et al., 2020; Russell et al., 2024). Furthermore, Young ORCA is characterized by strong, small-scale velocity lineations in the deep asthenosphere (below ~200 km depth) that are suggestive of small-scale convection in the region (Eilon et al., 2022), and Old ORCA is characterized by similarly strong velocity heterogeneity throughout the asthenosphere (100–300 km depth; Hariharan et al., 2025).

The three regions all have roughly similar values of anisotropy strength below the plates, with $|G|$ amplitudes that peak at about 3% and decrease with depth (Figure 10). These values suggest that whatever diversity of dynamic processes are active in the three regions, the strength of the resulting fabric that is coherent over ~500 km length scales is similar. In detail, the peak strength observed in the ORCA regions is shallower than beneath NoMelt; for the ORCAs, this places the strongest anisotropy within the narrow low-Q zone, while for NoMelt the peak falls near the base of the broader, more modestly attenuating region. The directions of anisotropy also differ; for Old ORCA, the fast direction within the strong-anisotropy region is aligned with plate motion, and Young ORCA shows a similar correspondence in the layered parameterization (Figure 9), but the direction of the strongest anisotropy beneath NoMelt is distinctly rotated from APM (Figure 10; Lin et al., 2016). These regional variations suggest that the low viscosities associated with a weak, low-Q asthenosphere may provide a critical environment for developing strong APM-induced fabric, effectively enabling more efficient Couette-style shear driven by plate motion into a narrow focused asthenospheric channel with high strain rates (Debayle et al., 2016). The higher Q and faster V_{SV} beneath NoMelt suggests stiffer upper asthenosphere that may result in a more broadly distributed zone of plate-driven Couette flow with lower strain rates combined with pressure driven plug-flow style deformation that rotates and pushes strain rate concentration to the deeper margin of the channel (e.g., Nagel et al., 2008; Semple & Lenardic, 2018; Wang et al., 2025). This interpretation is also consistent with localized anisotropy observations from the far western Pacific, where asthenospheric shear velocity and azimuthal anisotropy vary markedly over <1,000 km length scale, and anisotropy in the lower-velocity (presumably weaker) region is in much better agreement with APM than the higher-velocity (stiffer) region (Takeo et al., 2018).

Deeper in the asthenosphere (depth >200 km, below the low-Q channel), both regions display significant (1%–3%) anisotropy with fast directions that deviate from the directions that dominate the shallow asthenosphere. NoMelt anisotropy implies deep fabric that is largely east-west (~90°–110°), Old ORCA suggests fabric that is oriented NW–SE (~130°–150°), and Young ORCA has deep fabric roughly N–S (170°–190°). Assuming that the low-Q channel effectively absorbs the differential deformation between the plates and the deeper asthenosphere and decouples plate motion from the deep mantle, this deeper fabric presumably represents a localized, time-integrated (finite-strain) record of deformation induced directly by superposed pressure- or buoyancy-driven mantle flow at depth (reflecting some combination of present-day and prior differential strain). The regional differences highlighted here provide localized constraints on convection variations over inter-array distances of 2,000+ km.

Body-wave tomography at both ORCA arrays documents strong velocity heterogeneity that suggests small-scale convection (upwellings and downwellings) in the asthenosphere with length scales of ~200 km (Eilon et al., 2022; Hariharan et al., 2025). Our average anisotropy estimates do not capture an obvious signature of mantle fabric induced by this process, specifically either a weakening of azimuthal anisotropy in the upwelling and downwelling portions of the system (as proposed by Lin et al., 2016), or a strengthening of anisotropy at the base of the system where more horizontal deformation might be expected. We infer that our array-averaged models are dominated by the interaction of plate motion with the dynamically convecting asthenosphere, and that while locally the fabric will be complex and oriented with small-scale flow (e.g., Behn et al., 2007), the plate motion organizing that flow into rolls (e.g., Ballmer et al., 2010; Buck & Parmentier, 1986; Richter & Parsons, 1975) results in an array average dominated by significant horizontal shear. Furthermore, once a strong pre-existing anisotropic fabric has been formed, it may be difficult to overprint via transient and relatively localized convective features (e.g., Boneh et al., 2015; Boneh & Skemer, 2014; Kaminski & Ribe, 2002). Future evaluations of intra-array anisotropy estimates along with geodynamic modeling efforts may help address this issue.

6.2. Lithosphere-Asthenosphere Transition

The underlying parameters that control the rheological transition from lithosphere to asthenosphere (the so-called LAB) remain debated, with temperature, hydration and oxidation state, grain size, and the presence of partial melt all potentially playing a role (e.g., Rychert et al., 2020, and references therein). In our analysis, we identify thermal lithosphere depths of ~50 km (Young ORCA) and ~70 km (Old ORCA) based on the depth at which V_{SV} drops below ~4.4 km/s, which also approximately corresponds to the depth of the steepest negative gradient in V_{SV} (e.g., Fishwick, 2010; Rychert et al., 2020). The apparently gradual V_{SV} gradient we see is consistent with a transition driven by temperature. However, our broad surface wave phase velocity kernels preclude sensitivity to sharp gradients (cf. Bodin et al., 2012) and we cannot rule out sharp rheological transitions associated with gradients in hydration or melt (Evans et al., 2005; Naif et al., 2013). Although subject to the same resolution limitations, anisotropy provides an important complement to isotropic velocity as diagnostic of the LAB, particularly since it may be a more direct proxy for a gradient in rheology (e.g., Beghein et al., 2014; Lin et al., 2016; Nishimura & Forsyth, 1989; Yuan & Romanowicz, 2010).

At Old ORCA, we see an abrupt change in anisotropic direction observed between 60 and 80 km depth (Figure 9). There is also an abrupt change in the strength of anisotropy at around this depth (clearest in the layered parameterization). We interpret this change as marking the transition between active deformation fabric in the asthenosphere (Section 6.1), and ancient fabric locked into the lithosphere (Section 6.3), and suggest that it thus represents the rheological LAB. To evaluate the depth of this boundary objectively, we performed a grid search using a misfit test (Figure S14 in Supporting Information S1), and find that a discontinuity between 70 and 90 km provides adequate fit to the data. This depth is in good agreement with LAB depths derived from scattered waves in a variety of oceanic regions with plate ages greater than ~40 Ma (Kawakatsu et al., 2009; Kumar & Kawakatsu, 2011; Mark et al., 2021; Rychert et al., 2020; Schmerr, 2012), and it suggests that the modern rheological lithosphere is consistent with a proposed dehydration-controlled rheological lithosphere with a near-constant thickness (e.g., Evans et al., 2005; Gaherty et al., 1996; Hirth & Kohlstedt, 1996; Mark et al., 2021; Russell, Gaherty, et al., 2019; Sarafian et al., 2015). Russell, Gaherty, et al. (2019) invoke a dehydration-controlled mechanism to explain a similar anisotropy transition in NoMelt, where evidence for a dehydration boundary in the 70–90 depth range also comes from electromagnetic (Sarafian et al., 2015) and scattered-wave (Mark et al., 2021) observations. The argument is based on the correlation with the anisotropy boundary and the base of the decompression melting column at the mid-ocean ridge (Hirschmann, 2000; Klein & Langmuir, 1987), and the

10.1029/2025JB033545

premise that if lithospheric anisotropy were locked in by thermal cooling, it should progressively change to be more comparable to asthenospheric deformation at its base. The change in anisotropy strength and direction at Old ORCA are even more abrupt and occur at similar depth to that observed at NoMelt; however, the fact that Old ORCA does not clearly reflect FSD suggests that seafloor spreading is not the only process controlling deformation near the ridge in this region (see Section 6.3).

The continuous model for Young ORCA does not display abrupt changes with depth that could be interpreted as direct evidence of a lithosphere-asthenosphere boundary. This model provides the best fit to the data (Figure 6a), and to first order, it is more suggestive of thermal growth of the lithosphere, with FSD fabric only observed at very shallow depths associated with zero-age lithosphere and then fabric progressively rotating as the lithosphere thickens. The layered parameterization allows for an anisotropic boundary between 30 and 50 km (Figure S14 in Supporting Information S1), and the resulting anisotropic directions clearly separate into lithospheric and asthenospheric fabrics that are aligned with FSD and APM (Figure 9). This layered model is consistent with the lithosphere-dehydration hypothesis, although the depth is somewhat shallower than expected (Hirth & Kohlstedt, 1996). The next section offers further interpretation of the Young ORCA lithospheric fabric.

6.3. Lithospheric Fabric: Implications for Deformation at Spreading Centers

The models of lithospheric anisotropy for the ORCA experiment add to a growing set of observations (Eilon & Forsyth, 2020; Kawano et al., 2023; Russell & Gaherty, 2021; Saikia et al., 2021; Takeo et al., 2016, 2018; VanderBeek & Toomey, 2017) that suggest that mantle deformation at mid-ocean ridge spreading centers involves complexities beyond canonical models of spreading-parallel corner flow (e.g., Blackman et al., 2017; Blackman & Kendall, 2002), which predicts lithospheric anisotropy i.e. aligned with FSD (e.g., Mark et al., 2019; Raitt et al., 1969; Russell, Gaherty, et al., 2019). In both regions, the radial anisotropy in the shallow mantle with $V_{SH} > V_{SV}$ indicates horizontal alignment of orthorhombic olivine a-axes, consistent with corner-flow-induced fabric (e.g., Blackman & Kendall, 2002; Russell et al., 2022). At Young ORCA, the relatively strong $|G|$ with ψ_G approximately aligned with FSD above a depth of 30 km (and up to 50 km in the layered parameterization) further supports a strong corner-flow induced fabric, slightly weaker than, but otherwise comparable to, NoMelt. Young ORCA is characterized by a very fast spreading rate while NoMelt was formed at intermediate rate, so weaker fabric at Young ORCA implies that spreading rate may not be a major control on the strength of FSD fabric (Gaherty et al., 2004; Russell et al., 2022). The rapid rotation of fast anisotropy away from FSD in the deeper lithosphere (~30–60 km) in the smooth models implies deformation deep beneath the ridge crest that is not oriented in the seafloor-spreading direction, indicating that ridge-perpendicular deformation alone cannot fully explain lithospheric fabrics. This rotation may result from either progressive rotation of deformation at the base of the plate as the lithosphere aged and thickened, or from potentially transient periods of deformation oblique to spreading deeper beneath the ridge. This smooth model is slightly preferred by the data, but lacking improved observational constraints, the layered model offers a simpler interpretation.

In both Old ORCA subregions, mantle lithosphere anisotropy is anomalously weak, and significantly rotated (~30°) from FSD. The array also spans an abrupt change in seamount concentration and crustal thickness between its two subregions. The history of seafloor spreading (including age and spreading rate) is poorly known here, but our observations suggest atypical deformation processes at this region's formative MOR. If the array spans a section of seafloor that was undergoing an abrupt perturbation in spreading rate, the weak lithospheric fabric might owe to disorganized corner-flow (although radial anisotropy with $\xi > 1$ implies horizontally organized fabric, at least in the shallow lithosphere). Alternatively, the thicker crust and denser seamount census in the northwest region may result from a younger stage of secondary magmatism that modified and weakened the lithospheric fabric (Olugboji & Park, 2016; Wolfe & Solomon, 1998). However, this hypothesis would not explain why anisotropy is rotated from FSD and relatively weak in the southeast region as well. Another possibility is that FSD-skewed fabric could result from rapid motion of the MOR itself in a mantle reference frame in a sense that is oblique to seafloor spreading (Russell & Gaherty, 2021; VanderBeek & Toomey, 2017). In this scenario, the competition between corner flow and the lateral translation of the ridge through the mantle creates a complex, 3–D strain field. This competing shear prevents the development of a strong and coherent fabric, explaining the anomalously weak, misoriented azimuthal anisotropy. This would rotate the differential shear relative to the underlying asthenosphere away from FSD and would be consistent with the overall horizontal fabric implied by radial anisotropy $\xi > 1$ with similar strength as Young ORCA (Figure 7). While plate reconstruction models (e.g., GPlates) have proven useful for testing this scenario in other regions (Russell &

Gaherty, 2021), it is not possible to do so for Old ORCA due to the poorly constrained spreading history in this region (Section 2.2).

6.3.1. Crustal Fabric

In all three ORCA regional models, the oceanic crust is inferred to be anisotropic. Young ORCA is radially anisotropic but does not appear to require azimuthal anisotropy, while both Old ORCA subregions are best fit by the inclusion of both radial and azimuthal anisotropy, with the fast orientation of the azimuthal component roughly consistent with that in the underlying mantle. The sign and magnitude of crustal radial anisotropy ($V_{SH} \sim 4\%–7\%$ faster than V_{SV}) is very similar to that observed at NoMelt (Russell, Gaherty, et al., 2019), and is suggestive of either layered horizontal crustal lithologies or shear-induced fabric. Strongly foliated plagioclase fabric has been observed in some ophiolitic crust (e.g., VanTongeren et al., 2015). As discussed by Russell, Gaherty, et al. (2019), such anisotropy has not been widely observed in oceanic crust, but is in principle consistent with either the "gabbro glacier" (e.g., Morgan & Chen, 1993) or "sheeted sill" (Boudier et al., 1996) lower crustal accretion models. Arguably, the sheeted sill model (strong foliation, weak lineation) is most consistent with observations at NoMelt and Young ORCA of strong radial anisotropy ($V_{SH} > V_{SV}$) but no resolvable azimuthal anisotropy. By contrast, the measurable lower-crustal azimuthal anisotropy observed at Old ORCA may be more consistent with a gabbro glacier model, for which ductile flow (roughly perpendicular to the ridge) might produce more substantial lineation fabrics.

6.4. Comparison Between Local and Large-Scale Estimates of Anisotropy

Figure 10 shows depth profiles of ORCA regions and NoMelt, compared to depth profiles extracted from a global anisotropic model (Debayle et al., 2016) at the same locations. Figures S14 and S15 in Supporting Information S1 provide a broader comparison to additional basin-to-global scale models (Schaeffer et al., 2016; K. Yuan & Beghein, 2018). Because the large-scale models utilize a continuous, smooth parameterization with depth, we compare them to our smooth parameterization results. Global and plate-scale tomography models tend to significantly underestimate the strength of azimuthal anisotropy throughout the upper mantle, with average values in $|G|$ generally $\sim$0.5%–1.5% less than that observed in our ORCA models (Figure S14 in Supporting Information S1). In general, the global models do not attempt to model the upper lithosphere (models starting at 40–50 km depth), and thus they fail to capture the weak anisotropy at shallow depth at Old ORCA or the strong anisotropy at Young ORCA and NoMelt (Figure 10a; Figures S14a and S14c in Supporting Information S1). In the asthenosphere (100–200 km depth), Debayle et al. (2016) estimate $|G|$ and ψ_G that is in fairly good agreement (within $\sim$0.5% and $\pm 10°$) with the local-array-based models in most regions (Figure 10; Figures S15a and S15d in Supporting Information S1). In general, all of the global models better match the regional estimate of ψ_G than $|G|$, often agreeing to within $\pm 20°$ of the local-array-based estimates (Figures S14d–S14f in Supporting Information S1). However, upon closer inspection, the large-scale models fail to capture major details, such as the strong gradients in fast direction and their variability with depth that reflect distinct lithosphere and asthenosphere structure and dynamics (Sections 6.1–6.3), observed in all three of the local-array-based models. This can be seen directly in the surface-wave measurements; forward predictions of the strength and direction of 2θ Rayleigh-wave anisotropy calculated at the ORCA and NoMelt locations from all three large-scale models systemically misfit the observations in all regions across the period band 5–150 s (Figure S16 in Supporting Information S1). A similar conclusion emerges when comparing our local arrays to predictions from global geodynamic flow models (Figure S17 in Supporting Information S1). While models of the instantaneous strain axis (Conrad & Behn, 2010) capture some of the expected asthenospheric rotation, finite-strain models (Becker et al., 2008, 2014) do not reproduce the sharp variations in fast direction with depth and significantly overestimate the anisotropy strength.

The strong regional variation in anisotropy observed in the local-array-based models is consistent with a broader pattern of heterogeneous anisotropy observations seen in localized, OBS-based models worldwide (Saikia et al., 2021). Figure 11 summarizes the strength and direction of anisotropy at lithospheric and asthenospheric depths in several array-scale models spanning the ocean basins. Strength of anisotropy in the lithosphere varies from $\sim$1% to 6%, much larger than the range $\sim$1%–2% inferred from global models (e.g., Debayle et al., 2016; Schaeffer et al., 2016; K. Yuan & Beghein, 2018). Anisotropy in the asthenosphere is generally weaker, ranging from $\sim$1%–4%. Strong lithospheric anisotropy (relative to global models) has been noted previously (e.g., Russell, Gaherty, et al., 2019; Saikia et al., 2021; Takeo et al., 2018) and a fabric this strong is consistent with shear strain, presumably at the ridge, of up to 250%–400% (Russell et al., 2022). The global persistence of this strong fabric,

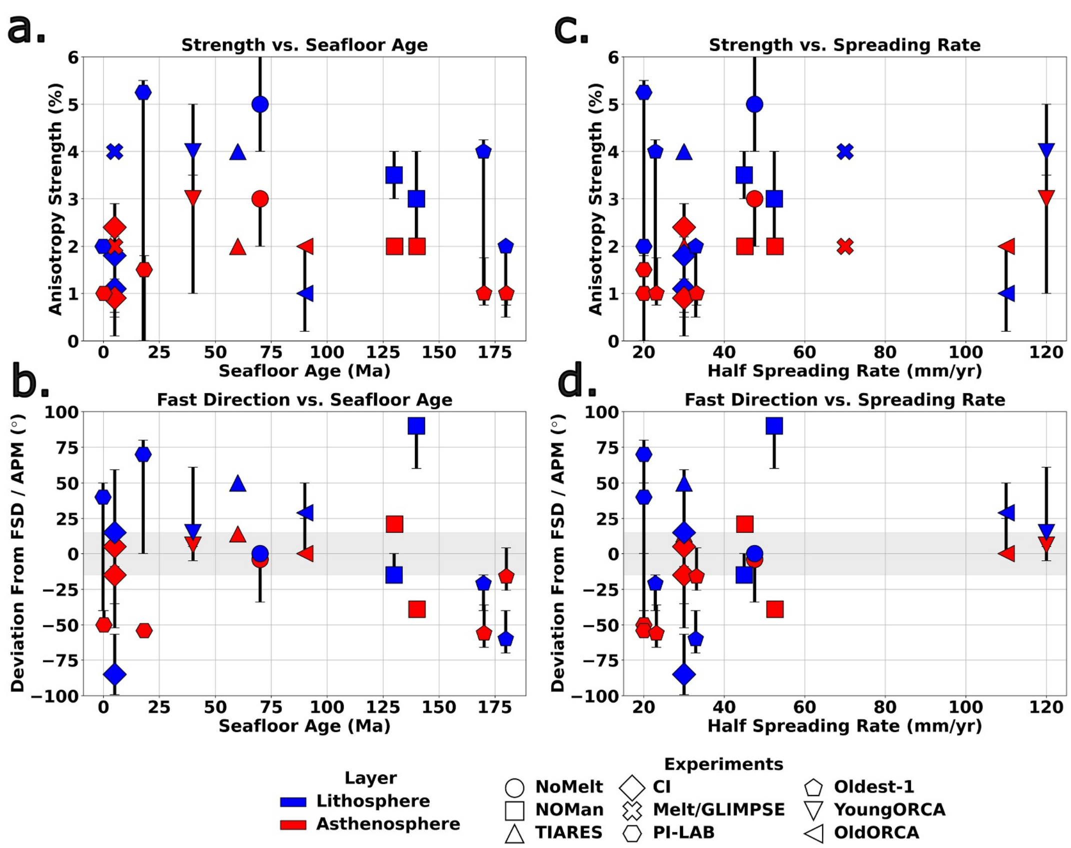

Figure 11. OBS regional array anisotropy strength and anisotropic fast-direction relative to respective FSD and APM, derived from surface-wave observations. Updated after Saikia et al. (2021), including vertical bars for the range of possible azimuths and strength in the lithosphere (blue; <60 km) and asthenosphere (red; >60 km) when present. Approximate average of lithosphere or asthenosphere taken as point location or when reported. In detail, data quality, frequency band, and modeling choices vary between studies, and the comparison is approximate. (a) Anisotropy magnitude relative to seafloor age and (b) fast direction deviation from either FSD (lithospheric depths) or APM (asthenosphere depths) relative to seafloor age. Shaded region is 20° acceptable angular misfit from Becker et al. (2014). (c) Anisotropy magnitude and (d) fast direction deviation relative to half spreading rate (mm/yr) and (c) fast direction deviation relative to half spreading rate (mm/yr). Cited experiments: NoMelt (Lin et al., 2016; Russell, Gaherty, et al., 2019); TIARES (Takeo et al., 2016); NOMan (Takeo et al., 2018); PI-LAB (Saikia et al., 2021); Cascadia Initiative (CI) (Eilon & Forsyth, 2020); Melt/GLIMPSE, note no fast direction (Rychert & Harmon, 2017); Oldest-1 (Kawano et al., 2023).

and particularly the near-ubiquitous finding at array-scale that the lithosphere is more strongly anisotropic than the asthenosphere, suggests that the strain produced by near-ridge convection and seafloor spreading (e.g., Blackman et al., 1996, 2017) is the dominant mode of deformation in the uppermost mantle. This mode is stronger and/or more coherent than deformation associated with plate-driven shear and/or convection in the asthenosphere, at least at length scales of several hundred km.

It is interesting to juxtapose this finding with global-scale models, and analyses thereof, that typically emphasize the large amplitude of both radial and azimuthal anisotropy in the asthenosphere (Beghein et al., 2014; Yuan & Beghein, 2018). These models indicate asthenospheric fabric which correlates both in strength (e.g., Debayle et al., 2016) and direction (e.g., Becker et al., 2014) with asthenospheric shear strain due to plate motion. This difference in emphasis arises from the spatial averaging and lack of shallow constraints inherent in many large-scale anisotropy analyses: they do an excellent job at capturing the asthenospheric shear produced by coherent, plate-scale deformation, but they have difficulty accurately resolving the upper lithosphere, and either the strength or direction of smaller-scale asthenospheric deformation processes, including those within mid-ocean spreading systems (subsequently recorded in the oceanic lithosphere). The local models suggest that such spreading-center deformation is paramount to dictating intraplate fabrics over length scales of ~400–1,000 km. As a corollary, the diminution of lithospheric anisotropy strength in models with broad spatial averaging implies that MOR processes are quite heterogeneous through space and time, imprinting oceanic plates with quite spatially variable fabrics.

7. Conclusions

Models of shear-wave anisotropy from the Young and Old ORCA arrays reveal a more complex picture of oceanic lithosphere-asthenosphere dynamics than is captured by large scale tomography. Azimuthal anisotropy beneath Young ORCA aligns with the FSD in the upper 20–30 km of the mantle, suggesting that corner-flow dominates deformation at shallow depths beneath the ridge. Old ORCA exhibits weak lithospheric anisotropy and fast-axis orientations rotated ∼30° from the inferred FSD in both subregions, perhaps because its formative MOR had absolute velocity that was large and misoriented relative to the spreading rate direction. A rapidly migrating ridge would induce a complex mantle flow field where the spreading-driven corner flow competes with oblique mantle shear, preventing the development of a strong fabric aligned with fossil spreading. These findings in the lithosphere underscore that processes responsible for local seafloor formation and evolution vary substantially over regional scales and can produce lithospheric fabrics that differ significantly from simple corner-flow models.

The lithosphere-asthenosphere transition is marked by decreases in V_{SV} and abrupt changes in $|G|$. At Young ORCA, this boundary (demarcated by $V_{SV} < 4.4$ km/s) is at ∼50 km depth, coincident with a gradual change in anisotropic orientation that may be thermally controlled. At Old ORCA the V_{SV} decrease is centered at ∼0 km depth, coincident with sharply defined transitions in ψ_G fast-axis direction and strength $|G|$. This change in fabric is more abrupt than would be expected from a thermally controlled growth of the lithosphere, and is more consistent with a dehydration-controlled rheological lithosphere. Abrupt anisotropy changes align well with independent scattered-wave estimates in similarly aged regions, lending support to a possible compositional contribution to rheological lithosphere thickness.

Beneath the LAB both ORCA regions exhibit strong asthenospheric anisotropy ($|G| \sim 2.5\%–3.5\%$) with fast axes oriented close to APM, indicating that plate-driven shear contributes significantly to mantle fabric within the low-viscosity asthenosphere. However, depth variations in both the strength and direction of anisotropy suggest that smaller-scale deformation processes driven by pressure and/or density variations contribute significantly to mantle deformation as well. Global-scale models only recover muted versions of these features, demonstrating the utility of dense, array-scale OBS deployments for mapping small-scale convective structures that are effectively averaged out at coarser resolutions.

Conflict of Interest

The authors declare no conflicts of interest relevant to this study.

Availability Statement

The seismic data from these experiments are available through the National Geophysical Facility Data Management Center (operated by EarthScope) under network code XE for Young ORCA and 7B for Old ORCA (Gaherty et al., 2019). Metadata for ORCA arrays catalogued with Eilon et al. (2021). All processing codes are openly available, most notably ambient noise processing code MATnoise (Russell, 2026b), the ASWMS-Q package for earthquake analysis (Russell & Jin, 2026), and inversion codes for azimuthal anisotropy (Russell, 2026a). Tabulated model files for both Young and Old ORCA are provided in Supporting Information S1 and available at Phillips (2025).

Acknowledgments

This research was supported by the National Science Foundation through NSF Grants OCE-1658491, OCE-1658214, OCE-1658070, and OCE-2051265. Some figures were made using GMT/PyGMT (Wessel et al., 2019). This research would not be possible without the fleet of OBS instruments managed by SIO and the crew and operators of the Kilo Moana and Roger Revelle research vessels that deployed and recovered the instruments. We acknowledge valuable editorial contributions from Göran Ekström, Donna Shillington, Ryan Porter, Helen Janiszewski, and Miles Bodmer, as well as editor Mark Behn, an Associate Editor, and two anonymous reviewers.

References

Adimah, N. I., Tan, Y. J., & Russell, J. B. (2024). Shear-wave velocity structure of the Blanco oceanic transform fault zone. *Geophysical Journal International*, *239*(2), 1287–1312. https://doi.org/10.1093/gji/ggae318

Aki, K. (1957). Space and time spectra of stationary stochastic waves, with special reference to microtremors. *Bulletin of the Earthquake Research Institute*, *35*(3), 415–456.

Auer, L., Becker, T. W., Boschi, L., & Schmerr, N. (2015). Thermal structure, radial anisotropy, and dynamics of oceanic boundary layers. *Geophysical Research Letters*, *42*(22), 9740–9749. https://doi.org/10.1002/2015GL066246

Ballmer, M. D., Ito, G., van Hunen, J., & Tackley, P. J. (2010). Small-scale sublithospheric convection reconciles geochemistry and geochronology of 'Superplume' volcanism in the western and south Pacific. *Earth and Planetary Science Letters*, *290*(1), 224–232. https://doi.org/10.1016/j.epsl.2009.12.025

Ballmer, M. D., Ito, G., Van Hunen, J., & Tackley, P. J. (2011). Spatial and temporal variability in Hawaiian hotspot volcanism induced by small-scale convection. *Nature Geoscience*, *4*(7), 457–460. https://doi.org/10.1038/ngeo1187

Ballmer, M. D., van Hunen, J., Ito, G., Tackley, P. J., & Bianco, T. A. (2007). Non-hotspot volcano chains originating from small-scale sub-lithospheric convection. *Geophysical Research Letters*, *34*(23), 1–5. https://doi.org/10.1029/2007GL031636

Becker, T. W., Conrad, C. P., Schaeffer, A. J., & Lebedev, S. (2014). Origin of azimuthal seismic anisotropy in oceanic plates and mantle. *Earth and Planetary Science Letters*, *401*, 236–250. https://doi.org/10.1016/j.epsl.2014.06.014

Becker, T. W., Kustowski, B., & Ekström, G. (2008). Radial seismic anisotropy as a constraint for upper mantle rheology. *Earth and Planetary Science Letters*, *267*(1), 213–227. https://doi.org/10.1016/j.epsl.2007.11.038

Beghein, C., Yuan, K., Schmerr, N., & Xing, Z. (2014). Changes in seismic Anisotropy shed light on the Nature of the Gutenberg discontinuity. *Science*, *343*(6176), 1237–1240. https://doi.org/10.1126/science.1246724

Behn, M. D., Hirth, G., & Kelemen, P. B. (2007). Trench-Parallel anisotropy produced by foundering of Arc lower crust. *Science*, *317*(5834), 108–111. https://doi.org/10.1126/science.1141269

Ben Ismaïl, W., & Mainprice, D. (1998). An olivine fabric database: An overview of upper mantle fabrics and seismic anisotropy. *Tectonophysics*, *296*(1), 145–157. https://doi.org/10.1016/S0040-1951(98)00141-3

Bensen, G. D., Ritzwoller, M. H., Barmin, M. P., Levshin, A. L., Lin, F., Moschetti, M. P., et al. (2007). Processing seismic ambient noise data to obtain reliable broad-band surface wave dispersion measurements. *Geophysical Journal International*, *169*(3), 1239–1260. https://doi.org/10.1111/j.1365-246X.2007.03374.x

Blackman, D. K., Boyce, D., Castelnau, O., Dawson, P., & Laske, G. (2017). Effects of crystal preferred orientation on upper-mantle flow near plate boundaries: Rheologic feedbacks and seismic anisotropy. *Geophysical Journal International*, *210*(3), 1481–1493. https://doi.org/10.1093/gji/ggx251

Blackman, D. K., & Kendall, J.-M. (2002). Seismic anisotropy in the upper mantle 2. Predictions for current plate boundary flow models. *Geochemistry, Geophysics, Geosystems*, *3*(9), 1–26. https://doi.org/10.1029/2001gc000247

Blackman, D. K., Kendall, J.-M., Dawson, P. R., Wenk, H.-R., Boyce, D., & Morgan, J. P. (1996). Teleseismic imaging of subaxial flow at mid-ocean ridges: Traveltime effects of anisotropic mineral texture in the mantle. *Geophysical Journal International*, *127*(2), 415–426. https://doi.org/10.1111/j.1365-246X.1996.tb04730.x

Bodin, T., Sambridge, M., Gallagher, K., & Rawlinson, N. (2012). Transdimensional inversion of receiver functions and surface wave dispersion. *Journal of Geophysical Research*, *117*(B2). https://doi.org/10.1029/2011JB008560

Bodmer, M., Toomey, D. R., Hooft, E. E., Nábělek, J., & Braunmiller, J. (2015). Seismic anisotropy beneath the Juan de Fuca plate system: Evidence for heterogeneous mantle flow. *Geology*, *43*(12), 1095–1098. https://doi.org/10.1130/G37181.1

Boneh, Y., Morales, L. F. G., Kaminski, E., & Skemer, P. (2015). Modeling olivine CPO evolution with complex deformation histories: Implications for the interpretation of seismic anisotropy in the mantle. *Geochemistry, Geophysics, Geosystems*, *16*(10), 3436–3455. https://doi.org/10.1002/2015GC005964

Boneh, Y., & Skemer, P. (2014). The effect of deformation history on the evolution of olivine CPO. *Earth and Planetary Science Letters*, *406*, 213–222. https://doi.org/10.1016/j.epsl.2014.09.018

Boudier, F., Nicolas, A., & Ildefonse, B. (1996). Magma chambers in the Oman ophiolite: Fed from the top and the bottom. *Earth and Planetary Science Letters*, *144*(1), 239–250. https://doi.org/10.1016/0012-821X(96)00167-7

Bowden, D. C., Kohler, M. D., Tsai, V. C., & Weeraratne, D. S. (2016). Offshore Southern California lithospheric velocity structure from noise cross-correlation functions. *Journal of Geophysical Research: Solid Earth*, *121*(5), 3415–3427. https://doi.org/10.1002/2016JB012919

Brunsvik, B., & Eilon, Z. (2023). Radial anisotropy in receiver function H-κ stacks. *Seismological Research Letters*, *95*(1), 479–487. https://doi.org/10.1785/0220230114

Buck, W. R. (1985). When does small-scale convection begin beneath oceanic lithosphere? *Nature*, *313*(6005), 775–777. https://doi.org/10.1038/313775a0

Buck, W. R., & Parmentier, E. M. (1986). Convection beneath young oceanic lithosphere: Implications for thermal structure and gravity (Pacific, Indian Ocean). *Journal of Geophysical Research*, *91*(B2), 1961–1974. https://doi.org/10.1029/JB091iB02p01961

Burgos, G., Montagner, J. P., Beucler, E., Capdeville, Y., Mocquet, A., & Drilleau, M. (2014). Oceanic lithosphere-asthenosphere boundary from surface wave dispersion data. *Journal of Geophysical Research: Solid Earth*, *119*(2), 1079–1093. https://doi.org/10.1002/2013JB010528

Christeson, G. L., Goff, J. A., & Reece, R. S. (2019). Synthesis of Oceanic crustal structure from two-dimensional seismic profiles. *Reviews of Geophysics*, *57*(2), 504–529. https://doi.org/10.1029/2019RG000641

Coffin, M. F., Duncan, R. A., Eldholm, O., Fitton, J. G., Frey, F. A., Larsen, H. C., et al. (2006). Large igneous provinces and scientific ocean drilling: Status quo and a look ahead. *Oceanography*, *19*(4), 150–160. https://doi.org/10.5670/oceanog.2006.13

Conrad, C. P., & Behn, M. D. (2010). Constraints on lithosphere net rotation and asthenospheric viscosity from global mantle flow models and seismic anisotropy. *Geochemistry, Geophysics, Geosystems*, *11*(5). https://doi.org/10.1029/2009GC002970

Conrad, C. P., & Hager, B. H. (2001). Mantle convection with strong subduction zones. *Geophysical Journal International*, *144*(2), 271–288. https://doi.org/10.1046/j.1365-246x.2001.00321.x

Crawford, W. C., & Webb, S. C. (2000). Identifying and removing tilt noise from low-frequency (<0.1 Hz) seafloor vertical seismic data. *Bulletin of the Seismological Society of America*, *90*(4), 952–963. https://doi.org/10.1785/0119990121

Debayle, E., Dubuffet, F., & Durand, S. (2016). An automatically updated S-wave model of the upper mantle and the depth extent of azimuthal anisotropy. *Geophysical Research Letters*, *43*(2), 674–682. https://doi.org/10.1002/2015GL067329

Debayle, E., & Ricard, Y. (2012). A global shear velocity model of the upper mantle from fundamental and higher Rayleigh mode measurements. *Journal of Geophysical Research*, *117*(B10). https://doi.org/10.1029/2012JB009288

Debayle, E., & Ricard, Y. (2013). Seismic observations of large-scale deformation at the bottom of fast-moving plates. *Earth and Planetary Science Letters*, *376*, 165–177. https://doi.org/10.1016/j.epsl.2013.06.025

Doran, A. K., & Laske, G. (2017). Ocean-bottom seismometer instrument orientations via automated rayleigh-wave arrival-angle measurements. *Bulletin of the Seismological Society of America*, *107*(2), 691–708. https://doi.org/10.1785/0120160165

Eagles, G. (2006). Deviations from an ideal thermal subsidence surface in the Southern Pacific ocean. *Terra Antartica Reports*, 109–118.

Eagles, G., Gohl, K., & Larter, R. D. (2004). High-resolution animated tectonic reconstruction of the South Pacific and West Antarctic Margin. *Geochemistry, Geophysics, Geosystems*, *5*(7). https://doi.org/10.1029/2003GC000657

Eakin, C. M., Rychert, C. A., & Harmon, N. (2018). The role of Oceanic transform faults in seafloor spreading: A global perspective from seismic Anisotropy. *Journal of Geophysical Research: Solid Earth*, *123*(2), 1736–1751. https://doi.org/10.1002/2017JB015176

Eddy, C. L., Ekström, G., & Nettles, M. (2022). Three-dimensional seismic anisotropy in the Pacific upper mantle from inversion of a surface-wave dispersion data set. *Geophysical Journal International*, *231*(1), 355–383. https://doi.org/10.1093/gji/ggac194

Eddy, C. L., Ekström, G., Nettles, M., & Gaherty, J. B. (2019). Age dependence and anisotropy of surface-wave phase velocities in the Pacific. *Geophysical Journal International*, *216*(1), 640–658. https://doi.org/10.1093/gji/ggy438

Eilon, Z. C., & Abers, G. A. (2017). High seismic attenuation at a mid-ocean ridge reveals the distribution of deep melt. *Science Advances*, *3*(5), e1602829. https://doi.org/10.1126/sciadv.1602829

Eilon, Z. C., & Forsyth, D. W. (2020). Depth-Dependent Azimuthal Anisotropy Beneath the Juan de Fuca Plate System. *Journal of Geophysical Research: Solid Earth*, *125*(8), e2020JB019477. https://doi.org/10.1029/2020JB019477

Eilon, Z. C., Gaherty, J. B., Zhang, L., Russell, J., McPeak, S., Phillips, J., et al. (2021). The Pacific OBS research into convecting asthenosphere (ORCA) experiment. *Seismological Research Letters*, *93*(1), 477–493. https://doi.org/10.1785/0220210173

Eilon, Z. C., Zhang, L., Gaherty, J. B., Forsyth, D. W., & Russell, J. B. (2022). Sub-Lithospheric small-scale convection tomographically imaged beneath the Pacific plate. *Geophysical Research Letters*, *49*(18), e2022GL100351. https://doi.org/10.1029/2022GL100351

Evans, R. L., Hirth, G., Baba, K., Forsyth, D., Chave, A., & Mackie, R. (2005). Geophysical evidence from the MELT area for compositional controls on oceanic plates. *Nature*, *437*(7056), 249–252. https://doi.org/10.1038/nature04014

Fishwick, S. (2010). Surface wave tomography: Imaging of the lithosphere–asthenosphere boundary beneath central and southern Africa? *Lithos*, *120*(1), 63–73. https://doi.org/10.1016/j.lithos.2010.05.011

Forsyth, D. W. (1975). The early structural evolution and anisotropy of the Oceanic upper mantle. *Geophysical Journal International*, *43*(1), 103–162. https://doi.org/10.1111/j.1365-246X.1975.tb00630.x

Forsyth, D. W., Harmon, N., Scheirer, D. S., & Duncan, R. A. (2006). Distribution of recent volcanism and the morphology of seamounts and ridges in the GLIMPSE study area: Implications for the lithospheric cracking hypothesis for the origin of intraplate, non-hot spot volcanic chains. *Journal of Geophysical Research*, *111*(11), 1–19. https://doi.org/10.1029/2005JB004075

Fraters, M. R. T., & Billen, M. I. (2021). On the implementation and usability of crystal preferred orientation evolution in geodynamic modeling. *Geochemistry, Geophysics, Geosystems*, *22*(10), e2021GC009846. https://doi.org/10.1029/2021GC009846

French, S. W., & Romanowicz, B. A. (2014). Whole-mantle radially anisotropic shear velocity structure from spectral-element waveform tomography. *Geophysical Journal International*, *199*(3), 1303–1327. https://doi.org/10.1093/gji/ggu334

Gaherty, J. B., Eilon, Z. C., Forsyth, D. W., & Ekström, G. (2019). PacificORCA. *International Federation of Digital Seismograph Networks*. https://doi.org/10.7914/SN/7B_2019

Gaherty, J. B., Jordan, T. H., & Gee, L. S. (1996). Seismic structure of the upper mantle in a central Pacific corridor. *Journal of Geophysical Research*, *101*(B10), 22291–22309. https://doi.org/10.1029/96jb01882

Gaherty, J. B., Lizarralde, D., Collins, J. A., Hirth, G., & Kim, S. (2004). Mantle deformation during slow seafloor spreading constrained by observations of seismic anisotropy in the western Atlantic. *Earth and Planetary Science Letters*, *228*(3–4), 255–265. https://doi.org/10.1016/j.epsl.2004.10.026

Goff, J. A., & Arbic, B. K. (2010). Global prediction of abyssal hill roughness statistics for use in ocean models from digital maps of paleo-spreading rate, paleo-ridge orientation, and sediment thickness. *Ocean Modelling*, *32*(1), 36–43. https://doi.org/10.1016/j.ocemod.2009.10.001

Gripp, A. E., & Gordon, R. G. (2002). Young tracks of hotspots and current plate velocities. *Geophysical Journal International*, *150*(2), 321–361. https://doi.org/10.1046/j.1365-246X.2002.01627.x

Gu, Y. J., Lerner-Lam, A. L., Dziewonski, A. M., & Ekström, G. (2005). Deep structure and seismic anisotropy beneath the East Pacific Rise. *Earth and Planetary Science Letters*, *232*(3), 259–272. https://doi.org/10.1016/j.epsl.2005.01.019

Hable, S., Sigloch, K., Barruol, G., Stähler, S. C., & Hadziioannou, C. (2018). Clock errors in land and ocean bottom seismograms: High-accuracy estimates from multiple-component noise cross-correlations. *Geophysical Journal International*, *214*(3), 2014–2034. https://doi.org/10.1093/gji/ggy236

Hariharan, A., Eilon, Z., Gaherty, J., Russell, J., Phillips, J., & Forsyth, D. (2025). Observations of small-scale heterogeneity in the upper mantle beneath old oceanic lithosphere. *Journal of Geophysical Research: Solid Earth*, *130*(12), e2025JB032002. https://doi.org/10.1029/2025JB032002

Hawley, W. B., Allen, R. M., & Richards, M. A. (2016). Tomography reveals buoyant asthenosphere accumulating beneath the Juan de Fuca plate. *Science*, *353*(6306), 1406–1408. https://doi.org/10.1126/science.aad8104

Hess, H. H. (1964). Seismic anisotropy of the uppermost mantle under Oceans. *Nature*, *203*(4945), 629–631. https://doi.org/10.1038/203629a0

Hirschmann, M. M. (2000). Mantle solidus: Experimental constraints and the effects of peridotite composition. *Geochemistry, Geophysics, Geosystems*, *1*(10). https://doi.org/10.1029/2000gc000070

Hirth, G., & Kohlstedt, D. L. (1996). Water in the oceanic upper mantle: Implications for rheology, melt extraction and the evolution of the lithosphere. *Earth and Planetary Science Letters*, *144*(1), 93–108. https://doi.org/10.1016/0012-821X(96)00154-9

Jackson, M. G., Becker, T. W., & Steinberger, B. (2021). Spatial characteristics of recycled and primordial reservoirs in the deep mantle. *Geochemistry, Geophysics, Geosystems*, *22*(3), e2020GC009525. https://doi.org/10.1029/2020GC009525

Janiszewski, H. A., Gaherty, J. B., Abers, G. A., Gao, H., & Eilon, Z. C. (2019). Amphibious surface-wave phase-velocity measurements of the Cascadia subduction zone. *Geophysical Journal International*, *217*(3), 1929–1948. https://doi.org/10.1093/gji/ggz051

Janiszewski, H. A., & Russell, J. B. (2025). Ambient noise analyses at Broadband ocean-bottom seismometers: Data quality and transfer function corrections. *Seismological Research Letters*, *97*(2A), 1048–1066. https://doi.org/10.1785/0220250106

Jin, G., & Gaherty, J. B. (2015). Surface wave phase-velocity tomography based on multichannel cross-correlation. *Geophysical Journal International*, *201*(3), 1383–1398. https://doi.org/10.1093/gji/ggv079

Kaminski, É., & Ribe, N. M. (2002). Timescales for the evolution of seismic anisotropy in mantle flow. *Geochemistry, Geophysics, Geosystems*, *3*(8), 1–17. https://doi.org/10.1029/2001gc000222

Kang, H., Kim, Y., Hung, S.-H., Lin, P.-Y. P., Isse, T., Kawakatsu, H., et al. (2023). Seismic velocity structure of upper mantle beneath the oldest Pacific seafloor: Insights from finite-frequency tomography. *Geochemistry, Geophysics, Geosystems*, *24*(9), e2022GC010833. https://doi.org/10.1029/2022GC010833

Karato, S.-i., Jung, H., Katayama, I., & Skemer, P. (2008). Geodynamic significance of seismic anisotropy of the upper mantle: New insights from laboratory studies. *Annual Review of Earth and Planetary Sciences*, *36*(1), 59–95. https://doi.org/10.1146/annurev.earth.36.031207.124120

Kawakatsu, H., Kumar, P., Takei, Y., Shinohara, M., Kanazawa, T., Araki, E., & Suyehiro, K. (2009). Seismic evidence for sharp lithosphere-asthenosphere boundaries of Oceanic plates. *Science*, *324*(5926), 499–502. https://doi.org/10.1126/science.1169499

Kawano, Y., Isse, T., Takeo, A., Kawakatsu, H., Morishige, M., Shiobara, H., et al. (2023). Seismic structure of the lithosphere-asthenosphere system beneath the oldest seafloor revealed by rayleigh-wave dispersion analysis. *Journal of Geophysical Research: Solid Earth*, *128*(6), e2023JB026529. https://doi.org/10.1029/2023JB026529

Klein, E. M., & Langmuir, C. H. (1987). Global correlations of ocean ridge basalt chemistry with axial depth and crustal thickness. *Journal of Geophysical Research*, *92*(B8), 8089–8115. https://doi.org/10.1029/jb092ib08p08089

Korenaga, T., Korenaga, J., Kawakatsu, H., & Yamano, M. (2021). A new reference model for the evolution of Oceanic lithosphere in a cooling Earth. *Journal of Geophysical Research: Solid Earth*, *126*(6), e2020JB021528. https://doi.org/10.1029/2020JB021528
Kreemer, C., Blewitt, G., & Klein, E. C. (2014). A geodetic plate motion and Global Strain Rate Model. *Geochemistry, Geophysics, Geosystems*, *15*(10), 3849–3889. https://doi.org/10.1002/2014GC005407
Kumar, P., & Kawakatsu, H. (2011). Imaging the seismic lithosphere-asthenosphere boundary of the oceanic plate. *Geochemistry, Geophysics, Geosystems*, *12*(1). https://doi.org/10.1029/2010GC003358
Kustowski, B., Ekström, G., & Dziewoński, A. M. (2008). Anisotropic shear-wave velocity structure of the Earth's mantle: A global model. *Journal of Geophysical Research*, *113*(B6). https://doi.org/10.1029/2007JB005169
Larter, R. D., Cunningham, A. P., Barker, P. F., Gohl, K., & Nitsche, F. O. (2002). Tectonic evolution of the Pacific margin of Antarctica 1. Late Cretaceous tectonic reconstructions. *Journal of Geophysical Research*, *107*(B12), EPM5-1–19. https://doi.org/10.1029/2000jb000052
Laske, G., Atkisson, G., Collins, J. A., & Blackman, D. K. (2026). Rayleigh waves from ohana obss in the northeast Pacific Ocean reveal low deep shear velocities and pervasive azimuthal anisotropy. *Journal of Geophysical Research: Solid Earth*, *131*(5), e2025JB032104. https://doi.org/10.1029/2025jb032104
Laske, G., Markee, A., Orcutt, J. A., Wolfe, C. J., Collins, J. A., Solomon, S. C., et al. (2011). Asymmetric shallow mantle structure beneath the Hawaiian Swell-evidence from Rayleigh waves recorded by the PLUME network. *Geophysical Journal International*, *187*(3), 1725–1742. https://doi.org/10.1111/j.1365-246X.2011.05238.x
Lin, F.-C., & Ritzwoller, M. H. (2010). Empirically determined finite frequency sensitivity kernels for surface waves. *Geophysical Journal International*, *182*(2), 923–932. https://doi.org/10.1111/j.1365-246X.2010.04643.x
Lin, F.-C., Ritzwoller, M. H., & Snieder, R. (2009). Eikonal tomography: Surface wave tomography by phase front tracking across a regional broad-band seismic array. *Geophysical Journal International*, *177*(3), 1091–1110. https://doi.org/10.1111/j.1365-246X.2009.04105.x
Lin, P.-Y. P., Gaherty, J. B., Jin, G., Collins, J. A., Lizarralde, D., Evans, R. L., & Hirth, G. (2016). High-resolution seismic constraints on flow dynamics in the oceanic asthenosphere. *Nature*, *535*(7613), 538–541. https://doi.org/10.1038/nature18012
Liu, X., & Ritzwoller, M. H. (2025). The effect of rayleigh–love coupling in an anisotropic medium. *Geophysical Journal International*, *241*(2), 1204–1225.
Lizarralde, D., Gaherty, J. B., Collins, J. A., Hirth, G., & Kim, S. D. (2004). Spreading-rate dependence of melt extraction at mid-ocean ridges from mantle seismic refraction data. *Nature*, *432*(7018), 744–747. https://doi.org/10.1038/nature03140
Long, M. D., & Becker, T. W. (2010). Mantle dynamics and seismic anisotropy. *Earth and Planetary Science Letters*, *297*(3–4), 341–354. https://doi.org/10.1016/j.epsl.2010.06.036
Long, M. D., & Silver, P. G. (2009). Mantle flow in subduction systems: The subslab flow field and implications for mantle dynamics. *Journal of Geophysical Research*, *114*(B10). https://doi.org/10.1029/2008JB006200
Luo, Y., Yang, Y., Zhao, K., Xu, Y., & Xia, J. (2015). Unraveling overtone interferences in love-wave phase velocity measurements by radon transform. *Geophysical Journal International*, *203*(1), 327–333. https://doi.org/10.1093/gji/ggv300
Ma, Z., Dalton, C. A., Russell, J. B., Gaherty, J. B., Hirth, G., & Forsyth, D. W. (2020). Shear attenuation and anelastic mechanisms in the central Pacific upper mantle. *Earth and Planetary Science Letters*, *536*, 116148. https://doi.org/10.1016/j.epsl.2020.116148
Mark, H. F., Collins, J. A., Lizarralde, D., Hirth, G., Gaherty, J. B., Evans, R. L., & Behn, M. D. (2021). Constraints on the depth, thickness, and strength of the G discontinuity in the central Pacific from S receiver functions. *Journal of Geophysical Research: Solid Earth*, *126*(4), e2019JB019256. https://doi.org/10.1029/2019JB019256
Mark, H. F., Lizarralde, D., Collins, J. A., Miller, N. C., Hirth, G., Gaherty, J. B., & Evans, R. L. (2019). Azimuthal seismic anisotropy of 70-Ma pacific-plate upper mantle. *Journal of Geophysical Research: Solid Earth*, *124*(2), 1889–1909. https://doi.org/10.1029/2018JB016451
Matthews, K. J., Mller, R. D., Wessel, P., & Whittaker, J. M. (2011). The tectonic fabric of the ocean basins. *Journal of Geophysical Research*, *116*(12), 1–28. https://doi.org/10.1029/2011JB008413
Mazzullo, A., Stutzmann, E., Montagner, J.-P., Kiselev, S., Maurya, S., Barruol, G., & Sigloch, K. (2017). Anisotropic Tomography Around La Réunion Island From Rayleigh Waves. *Journal of Geophysical Research: Solid Earth*, *122*(11), 9132–9148. https://doi.org/10.1002/2017JB014354
Menke, W., & Jin, G. (2015). Waveform fitting of cross spectra to determine phase velocity using Aki's formula. *Bulletin of the Seismological Society of America*, *105*(3), 1619–1627. https://doi.org/10.1785/0120140245
Montagner, J. P. (2002). Upper mantle low anisotropy channels below the Pacific Plate. *Earth and Planetary Science Letters*, *202*(2), 263–274. https://doi.org/10.1016/S0012-821X(02)00791-4
Montagner, J.-P., & Anderson, D. L. (1989). Petrological constraints on seismic anisotropy. *Physics of the Earth and Planetary Interiors*, *54*(1), 82–105. https://doi.org/10.1016/0031-9201(89)90189-1
Montagner, J. P., & Nataf, H.-C. (1986). A simple method for inverting the azimuthal anisotropy of surface waves. *Journal of Geophysical Research*, *91*(B1), 511–520. https://doi.org/10.1029/jb091ib01p00511
Montagner, J.-P., & Tanimoto, T. (1990). Global anisotropy in the upper mantle inferred from the regionalization of phase velocities. *Journal of Geophysical Research*, *95*(B4), 4797–4819. https://doi.org/10.1029/JB095iB04p04797
Montagner, J.-P., & Tanimoto, T. (1991). Global upper mantle tomography of seismic velocities and anisotropies. *Journal of Geophysical Research*, *96*(B12), 20337–20351. https://doi.org/10.1029/91JB01890
Morgan, J. P., & Chen, Y. J. (1993). The genesis of oceanic crust: Magma injection, hydrothermal circulation, and crustal flow. *Journal of Geophysical Research*, *98*(B4), 6283–6297. https://doi.org/10.1029/92JB02650
Mortimer, N., van den Bogaard, P., Hoernle, K., Timm, C., Gans, P. B., Werner, R., & Riefstahl, F. (2019). Late Cretaceous oceanic plate reorganization and the breakup of Zealandia and Gondwana. *Gondwana Research*, *65*, 31–42. https://doi.org/10.1016/j.gr.2018.07.010
Müller, R. D., Sdrolias, M., Gaina, C., & Roest, W. R. (2008). Age, spreading rates, and spreading asymmetry of the world's ocean crust. *Geochemistry, Geophysics, Geosystems*, *9*(4), 1–19. https://doi.org/10.1029/2007GC001743
Nagel, T. J., Ryan, W. B. F., Malinverno, A., & Buck, W. R. (2008). Pacific trench motions controlled by the asymmetric plate configuration. *Tectonics*, *27*(3). https://doi.org/10.1029/2007TC002183
Naif, S., Key, K., Constable, S., & Evans, R. L. (2013). 3). Melt-rich channel observed at the lithosphere–asthenosphere boundary. *Nature*, *495*(7441), 356–359. https://doi.org/10.1038/nature11939
Nakajima, J., & Hasegawa, A. (2004). Shear-wave polarization anisotropy and subduction-induced flow in the mantle wedge of northeastern Japan. *Earth and Planetary Science Letters*, *225*(3), 365–377. https://doi.org/10.1016/j.epsl.2004.06.011
Nishimura, C. E., & Forsyth, D. W. (1989). The anisotropic structure of the upper mantle in the Pacific. *Geophysical Journal International*, *96*(2), 203–229. https://doi.org/10.1111/j.1365-246X.1989.tb04446.x
Olugboji, T. M., & Park, J. (2016). Crustal anisotropy beneath Pacific Ocean-Islands from harmonic decomposition of receiver functions. *Geochemistry, Geophysics, Geosystems*, *17*(3), 810–832. https://doi.org/10.1002/2015GC006166

Peselnick, L., & Nicolas, A. (1978). Seismic anisotropy in an ophiolite peridotite: Application to oceanic upper mantle. *Journal of Geophysical Research*, *83*(B3), 1227–1235. https://doi.org/10.1029/JB083iB03p01227

Phillips, J. (2025). Spatial variation in anisotropic shear velocity of oceanic lithosphere-asthenosphere in the Pacific [Dataset]. *Zenodo*. https://doi.org/10.5281/zenodo.17805266

Phillips, J., Gaherty, J. B., Russell, J. B., Eilon, Z., Forsyth, D. W., & Byrnes, J. S. (2024). Oceanic crustal thickness variation revealed by joint gravity and seismic inversions across the Pacific, pp. S31C–3246).

Raitt, R. W., Shor, G. G., Jr., Francis, T. J. G., & Morris, G. B. (1969). Anisotropy of the Pacific upper mantle. *Journal of Geophysical Research*, *74*(12), 3095–3109. https://doi.org/10.1029/JB074i012p03095

Ribe, N. M. (1989). Seismic anisotropy and mantle flow. *Journal of Geophysical Research*, *94*(B4), 4213–4223. https://doi.org/10.1029/JB094iB04p04213

Richter, F. M., & Parsons, B. (1975). On the interaction of two scales of convection in the mantle. *Journal of Geophysical Research*, *80*(17), 2529–2541. https://doi.org/10.1029/JB080i017p02529

Russell, J. B. (2026a). Jbrussell/invswani-gbhe: Release v1.0.0 [Software]. *Zenodo*. https://doi.org/10.5281/zenodo.18931086

Russell, J. B. (2026b). Jbrussell/matnoise: Release v1.0.0 [Software]. *Zenodo*. https://doi.org/10.5281/zenodo.18931060

Russell, J. B., Dalton, C. A., Havlin, C., Holtzman, B. K., Eilon, Z., Gaherty, J. B., & Forsyth, D. W. (2024). Reduced grain size in Oceanic asthenosphere and implications for mantle dynamics, pp. DI51A–3048).

Russell, J. B., Eilon, Z., & Mosher, S. G. (2019b). Obsrange: A new tool for the precise remote location of OceanBottom seismometers. *Seismological Research Letters*, *90*(4), 1627–1641. https://doi.org/10.1785/0220180336

Russell, J. B., & Gaherty, J. B. (2021). Lithosphere structure and seismic anisotropy offshore Eastern North America: Implications for Continental breakup and ultra-slow spreading dynamics. *Journal of Geophysical Research: Solid Earth*, *126*(12), 1–30. https://doi.org/10.1029/2021JB022955

Russell, J. B., Gaherty, J. B., Lin, P. Y. P., Lizarralde, D., Collins, J. A., Hirth, G., & Evans, R. L. (2019). High-resolution constraints on Pacific upper mantle petrofabric inferred from surface-wave anisotropy. *Journal of Geophysical Research: Solid Earth*, *124*(1), 631–657. https://doi.org/10.1029/2018JB016598

Russell, J. B., Gaherty, J. B., Mark, H. F., Hirth, G., Hansen, L. N., Lizarralde, D., et al. (2022). Seismological evidence for girdled olivine lattice-preferred orientation in Oceanic lithosphere and implications for mantle deformation processes during seafloor spreading. *Geochemistry, Geophysics, Geosystems*, *23*(10), e2022GC010542. https://doi.org/10.1029/2022GC010542

Russell, J. B., & Jin, G. (2026). Jbrussell/aswms-q: Release v1.0.0 [Software]. *Zenodo*. https://doi.org/10.5281/zenodo.18931064

Rychert, C. A., Harmon, N., Constable, S., & Wang, S. (2020). The nature of the lithosphere-asthenosphere boundary. *Journal of Geophysical Research: Solid Earth*, *125*(10), 1–39. https://doi.org/10.1029/2018JB016463

Rychert, C. A., & Harmon, N. (2017). Constraints on the anisotropic contributions to velocity discontinuities at 60 km depth beneath the Pacific. *Geochemistry, Geophysics, Geosystems*, *18*(8), 2855–2871. https://doi.org/10.1002/2017GC006850

Saikia, U., Rychert, C., Harmon, N., & Kendall, J. M. (2021). Upper mantle anisotropic shear velocity structure at the equatorial mid-atlantic ridge constrained by Rayleigh Wave Group velocity analysis from the PI-LAB experiment. *Geochemistry, Geophysics, Geosystems*, *22*(3), e2020GC009495. https://doi.org/10.1029/2020GC009495

Sandwell, D. T., Harper, H., Tozer, B., & Smith, W. H. (2021). Gravity field recovery from geodetic altimeter missions. *Advances in Space Research*, *68*(2), 1059–1072. https://doi.org/10.1016/j.asr.2019.09.011

Sarafian, E., Evans, R. L., Collins, J. A., Elsenbeck, J., Gaetani, G. A., Gaherty, J. B., et al. (2015). The electrical structure of the central Pacific upper mantle constrained by the NoMelt experiment. *Geochemistry, Geophysics, Geosystems*, *16*(4), 1115–1132. https://doi.org/10.1002/2014GC005709

Schaeffer, A., Lebedev, S., & Becker, T. (2016). Azimuthal seismic anisotropy in the Earth's upper mantle and the thickness of tectonic plates. *Geophysical Journal International*, *207*(2), 901–933. https://doi.org/10.1093/gji/ggw309

Schmerr, N. (2012). The gutenberg discontinuity: Melt at the lithosphere-asthenosphere boundary. *Science*, *335*(6075), 1480–1483. https://doi.org/10.1126/science.1215433

Semple, A. G., & Lenardic, A. (2018). Plug flow in the Earth's asthenosphere. *Earth and Planetary Science Letters*, *496*, 29–36. https://doi.org/10.1016/j.epsl.2018.05.030

Seton, M., Müller, R. D., Zahirovic, S., Williams, S., Wright, N. M., Cannon, J., et al. (2020). A global data set of present-day Oceanic crustal age and seafloor spreading parameters. *Geochemistry, Geophysics, Geosystems*, *21*(10), 1–15. https://doi.org/10.1029/2020GC009214

Silver, P. G., & Holt, W. E. (2002). The mantle flow field beneath Western North America. *Science*, *295*(5557), 1054–1057. https://doi.org/10.1126/science.1066878

Stixrude, L., & Lithgow-Bertelloni, C. (2012). Geophysics of chemical heterogeneity in the mantle. *Annual Review of Earth and Planetary Sciences*, *40*(1), 569–595. https://doi.org/10.1146/annurev.earth.36.031207.124244

Takeo, A., Forsyth, D. W., Weeraratne, D. S., & Nishida, K. (2014). Estimation of azimuthal anisotropy in the NW Pacific from seismic ambient noise in seafloor records. *Geophysical Journal International*, *199*(1), 11–22. https://doi.org/10.1093/gji/ggu240

Takeo, A., Kawakatsu, H., Isse, T., Nishida, K., Shiobara, H., Sugioka, H., et al. (2018). In situ characterization of the lithosphere-asthenosphere system beneath NW Pacific Ocean via broadband dispersion survey with two OBS arrays. *Geochemistry, Geophysics, Geosystems*, *19*(9), 3529–3539. https://doi.org/10.1029/2018GC007588

Takeo, A., Kawakatsu, H., Isse, T., Nishida, K., Sugioka, H., Ito, A., et al. (2016). Seismic azimuthal anisotropy in the oceanic lithosphere and asthenosphere from broadband surface wave analysis of OBS array records at 60 Ma seafloor. *Journal of Geophysical Research: Solid Earth*, *121*(3), 1927–1947. https://doi.org/10.1002/2015JB012429

Trabant, C., Hutko, A. R., Bahavar, M., Karstens, R., Ahern, T., & Aster, R. (2012). Data products at the IRIS DMC: Stepping stones for research and other applications. *Seismological Research Letters*, *83*(5), 846–854. https://doi.org/10.1785/0220120032

VanderBeek, B. P., & Toomey, D. R. (2017). Shallow Mantle Anisotropy Beneath the Juan de Fuca Plate. *Geophysical Research Letters*, *44*(22), 11382–11389. https://doi.org/10.1002/2017GL074769

VanTongeren, J. A., Hirth, G., & Kelemen, P. B. (2015). Constraints on the accretion of the gabbroic lower oceanic crust from plagioclase lattice preferred orientation in the Samail ophiolite. *Earth and Planetary Science Letters*, *427*, 249–261. https://doi.org/10.1016/j.epsl.2015.07.001

Wang, Z. R., Conrad, C. P., Lebedev, S., Iaffaldano, G., & Hopper, J. R. (2025). Depth-dependent azimuthal seismic anisotropy governed by Couette/Poiseuille flow partitioning in the asthenosphere. *Earth and Planetary Science Letters*, *667*, 119527. https://doi.org/10.1016/j.epsl.2025.119527

Wessel, P., Luis, J. F., Uieda, L., Scharroo, R., Wobbe, F., Smith, W. H. F., & Tian, D. (2019). The generic mapping tools version 6. *Geochemistry, Geophysics, Geosystems*, *20*(11), 5556–5564. https://doi.org/10.1029/2019GC008515

Wolfe, C. J., & Solomon, S. C. (1998). Shear-wave splitting and implications for mantle flow beneath the MELT Region of the East Pacific rise. *Science*, *280*(5367), 1230–1232. https://doi.org/10.1126/science.280.5367.1230

Yang, X., Luo, Y., Xu, H., & Zhao, K. (2020). Shear wave velocity and radial anisotropy structures beneath the central Pacific from surface wave analysis of OBS records. *Earth and Planetary Science Letters*, *534*, 116086. https://doi.org/10.1016/j.epsl.2020.116086

Yoshimura, Y. (2022). The Cretaceous normal superchron: A mini-review of its discovery, short reversal events, paleointensity, paleosecular variations, paleoenvironment, volcanism, and mechanism. *Frontiers in Earth Science*, *10*, 834024. https://doi.org/10.3389/feart.2022.834024

Yuan, H., & Romanowicz, B. (2010). Depth dependent azimuthal anisotropy in the western US upper mantle. *Earth and Planetary Science Letters*, *300*(3), 385–394. https://doi.org/10.1016/j.epsl.2010.10.020

Yuan, K., & Beghein, C. (2018). A Bayesian method to quantify azimuthal anisotropy model uncertainties: Application to global azimuthal anisotropy in the upper mantle and transition zone. *Geophysical Journal International*, *213*(1), 603–622. https://doi.org/10.1093/gji/ggy004

Zhang, S., & Karato, S.-i. (1995). Lattice preferred orientation of olivine aggregates deformed in simple shear. *Nature*, *375*(6534), 774–777. https://doi.org/10.1038/375774a0